Nutrient and salt depletion synergistically boosts glucose metabolism in individual bacteria

Georgina Glover[1,2], Margaritis Voliotis[1,3], Urszula Łapińska[1,4], Brandon M. Invergo[5], Darren Soanes[4], Paul O'Neill[4], Karen Moore[4], Nela Nikolic[1,6], Peter G. Petrov[2], David S. Milner[7], Sumita Roy[1,4], Kate Heesom[8], Thomas A. Richards[7], Krasimira Tsaneva-Atanasova[1,3,9] & Stefano Pagliara[1,4]*.

1. Living Systems Institute, University of Exeter, Stocker Road, Exeter EX4 4QD, UK.
2. Department of Physics and Astronomy, University of Exeter, Stocker Road, Exeter EX4 4QL, UK.
3. Department of Mathematics, University of Exeter, Stocker Road, Exeter, UK.
4. Biosciences, University of Exeter, Stocker Road, Exeter EX4 4Q, UK.
5. Translational Research Exchange at Exeter, University of Exeter, Exeter, United Kingdom
6. Institute of Science and Technology Austria, 3400 Klosterneuburg, Austria.
7. Department of Zoology, University of Oxford, 11a Mansfield Road, Oxford OX1 3SZ, UK
8. University of Bristol Proteomics Facility, University Walk, Bristol BS8 1TD, UK
9. Dept. of Bioinformatics and Mathematical Modelling, Institute of Biophysics and Biomedical Engineering, Bulgarian Academy of Sciences, 105 Acad. G. Bonchev Str., 1113 Sofia, Bulgaria

Correspondence: email: S.Pagliara@exeter.ac.uk

ABSTRACT

The interaction between a cell and its environment shapes fundamental intracellular processes such as cellular metabolism. In most cases growth rate is treated as a proximal metric for understanding the cellular metabolic status. However, changes in growth rate might not reflect metabolic variations in individuals responding to environmental fluctuations. Here we use single-cell microfluidics-microscopy combined with transcriptomics, proteomics and mathematical modelling to quantify the accumulation of glucose within *Escherichia coli* cells. In contrast to the current consensus, we reveal that environmental conditions which are comparatively unfavourable for growth, where both nutrients and salinity are depleted, increase glucose accumulation rates in individual bacteria and population subsets. We find that these changes in metabolic function are underpinned by variations at the translational and posttranslational level but not at the transcriptional level and are not dictated by changes in cell size. The metabolic response-characteristics identified greatly advance our fundamental understanding of the interactions between bacteria and their environment and have important ramifications when investigating cellular processes where salinity plays an important role.

38 **INTRODUCTION**

39 All core metabolic networks require the uptake and utilization of carbon sources. Such function
40 is variant, adaptable and in the process of being precisely shaped by natural selection as many
41 heterotrophic organisms need to adapt their metabolic capabilities to dwell in scarce nutrient
42 environments[1–4]. In the case of bacteria, sugars often represent the primary driving force for
43 growth; they are used to power replication, to make storage compounds, and/or for the
44 production of secondary metabolites that further dictate metabolic function[5,6]. Glucose is
45 commonly employed to investigate the regulation of sugar uptake and metabolism in
46 bacteria[7]. In fact, many bacterial species primarily use glucose when exposed to nutrient
47 mixtures[8,9] and have evolved several independent ways of acquiring glucose from the
48 environment, as characterised by hundreds of variant glucose transport systems[8].

49 In gram-negative bacteria, such as *Escherichia coli*, glucose passively diffuses through
50 outer membrane porins whose expression is regulated both at the transcriptional and
51 translational level[10–12]. Glucose then crosses the *E. coli* inner membrane via five different
52 permeases including the glucose and mannose phosphotransferase systems (PTS)[8],[13]. Once
53 in the cytoplasm glucose is phosphorylated to glucose-6-phosphate that is broken down to
54 pyruvate, this in turn is metabolised to acetyl-CoA which then enters the citric acid cycle[14]
55 generating ATP. At micromolar extracellular concentrations, glucose and its fluorescent
56 analogue 2-(N-(7-Nitrobenz-2-oxa-1,3-diazol-4-yl)Amino)-2-Deoxyglucose (2-NBDG)
57 transiently accumulate intracellularly as a result of concomitant uptake and degradation
58 processes[15]. Seminal experiments carried out in chemostats suggest that glucose uptake
59 increases with cell surface area[5,15–17] and it is heterogeneous within clonal *E. coli*
60 populations.

61 These insights were obtained by employing bacteria growing in optimal conditions or
62 at low nutrient levels[15]. In contrast, in natural environments changes in other parameters are

63 common place[18–24]. For example, the salinity of aquatic ecosystems is changing
64 worldwide[25], it has been rated as one of the most important environmental changes[26] and
65 can have a profound impact on microbial growth and infectivity[27,28], thus affecting
66 biodiversity[29]. Salinity is decreasing in naturally saline ecosystems due to increased
67 agricultural drainages and unusual wind patterns[30], whereas the salinity of freshwater
68 ecosystems is increasing due to de-icing or salt mining (up to 97% increase[29]), along with
69 climatic aridification and rising sea levels[25]. Furthermore, salinity can dramatically change
70 across different bodily environments with a ~7-fold decrease in NaCl content from the colon
71 to the ileum (i.e from 6.1 to 0.9 g/L)[31–33] or across different humans with a 40% increase in
72 the lungs of cystic fibrosis patients[34]. These salinity variations often occur concomitantly
73 other environmental variations, such as changes in temperature, pH or nutrient levels, which
74 can result in additive, antagonistic or synergistic effects on microbes including *Escherichia*
75 *coli*[35,36]. Variations in temperature or content of metals have frequently been investigated
76 in combination with salinity, whereas changes in the nutrient-salinity pair has received less
77 attention[35]. Understanding and predicting the effects of multiple environmental variations
78 on the phenotypic diversity in microbial traits, such as metabolic rates, is critical for unravelling
79 how microbes function in their environment.

80 Here we study the diversity in glucose metabolism within clonal *E. coli* populations
81 and show that simultaneous extracellular nutrient and salt depletion synergistically enhance
82 glucose metabolism. These single-cell traits are not displayed when bacteria are exposed to
83 nutritional or salinity depletion alone, demonstrating that the effect of these environmental
84 changes on glucose metabolism is not additive. These changes in metabolic function are
85 underpinned by variations at the translational and posttranslational level but not at the
86 transcriptional level and are not dictated by changes in cell size. These findings offer unique
87 understanding of the interaction between a cell and its environment and will inform modelling

88 metabolic flux across bacterial populations[6], adjusting process parameters in biotechnology,
89 food preservation or metabolic engineering[37] and optimizing treatment with antibiotics that
90 utilize sugar uptake pathways to reach their intracellular target[38–40].
91

92 **RESULTS**

93 ***Experimental assessment of glucose accumulation and degradation in individual bacteria***

94 In order to quantify glucose uptake and accumulation in individual bacteria, we introduced a
95 clonal *E. coli* population into a microfluidic mother machine device[41]. This device is
96 equipped with a large microfluidic chamber for bacteria loading and media delivery via
97 pressure-driven microfluidics, connected with thousands of bacteria hosting channels with
98 cross section comparable to individual bacteria (inset in Fig. 1).

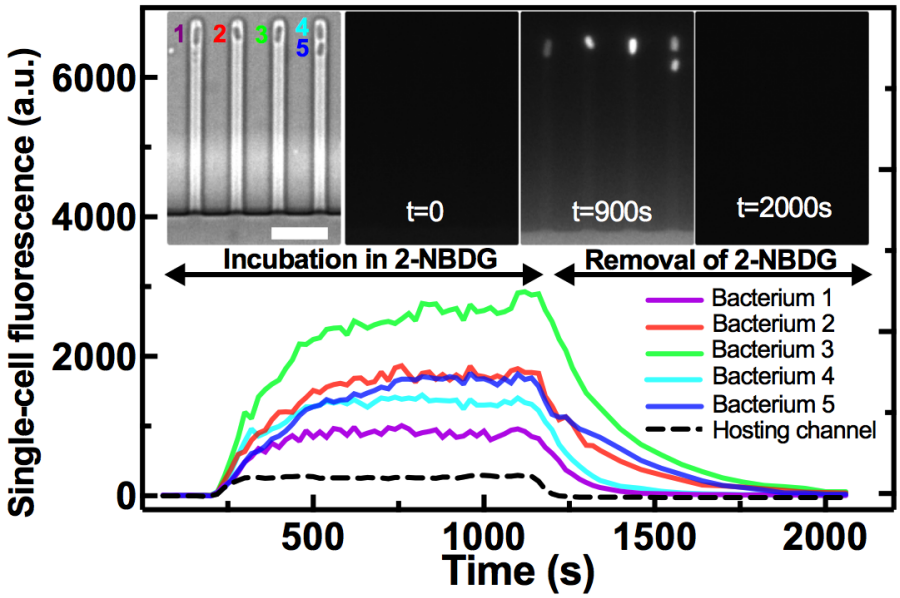

99

100 **Figure 1. Experimental assessment of glucose accumulation and degradation in**
101 **individual bacteria.** Temporal dependence of the intracellular fluorescence of the glucose
102 analogue 2-NBDG in five representative *E. coli* cells confined in the bacterial hosting channels
103 of the microfluidic mother machine. The dashed line represents the fluorescence of the
104 extracellular 2-NBDG in the bacterial hosting channels. Noteworthy, we measured 2-NBDG
105 fluorescence as the mean fluorescent values of each pixel constituting each bacterium, thus
106 normalizing by cell size. Insets from left to right: brightfield image of the five bacteria at t=0 s
107 when the fluorescent glucose analogue is added to the mother machine; corresponding image
108 in the green fluorescent channel; saturation of 2-NBDG intracellular fluorescence levels at
109 t=900 s followed by removal of extracellular 2-NBDG at t=1200 s; complete degradation of

110 intracellular 2-NBDG leading to intracellular fluorescence down to background levels by
111 t=2000 s. Scale bar: 5 μm.
112
113 We then added 30 μM 2-NBDG (i.e. a fluorescent glucose analogue) dissolved in glucose-free
114 M9 medium[5,15] in the microfluidic chamber while measuring its diffusion in the bacteria
115 hosting channels over time (dashed line in Fig. 1). We measured a progressive increase in the
116 fluorescence of individual bacteria that quickly became brighter than the channel fluorescence
117 (solid lines in Fig. 1 and insets) demonstrating higher intracellular compared to extracellular 2-
118 NBDG concentration. This was due to the uptake of 2-NBDG and subsequent accumulation in
119 single bacteria up to a steady-state[5,15,42,43]. This hyperbolic accumulation kinetics
120 indicated the presence of a sink term, namely intracellular phosphorylation of 2-NBDG and its
121 degradation by *E. coli*, processes that are comparable between glucose and 2-NBDG[5,42].
122 To gain further insight of the dynamics of this degradation process, the extracellular 2-
123 NBDG was washed away from the microfluidic chamber at t=1200 s and replaced with fresh
124 LB medium. Consequently, we measured an exponential decrease in the fluorescence of both
125 the bacteria hosting channels and of each bacterium (dashed and solid lines, respectively, in
126 Fig. 1 and insets). This rapid decrease could not be accounted for by dilution due to cell
127 growth[5,44].
128 In order to quantify phenotypic heterogeneity in glucose accumulation, we evaluated
129 the coefficient of variation (CV, the ratio between the standard deviation and the mean) of
130 single-bacterium 2-NBDG fluorescence values across the clonal population at each time point.
131 We verified that this heterogeneity could not be attributed to anisotropy in 2-NBDG
132 concentration within the bacteria hosting channels (Fig. S1 and Table S1)[41].
133
134 ***Glucose accumulation is maximal under simultaneous nutritional and salinity depletion***
135 We then used the experimental approach above to determine the impact of nutritional and
136 salinity depletion on glucose accumulation. We pre-cultured *E. coli* in three environments with

137 three different salt contents broadly recapitulating the salinity encountered by bacteria in
138 mesohaline (10 g/L NaCl), oligohaline (5 g/L NaCl) or fresh (0.5 g/L NaCl) water[29]. These
139 salinity variations also approximate the NaCl concentration faced by bacteria in the colonic or
140 the ileal environment (6.1 and 0.9 g/L NaCl, respectively)[32]. Moreover, at the lowest salinity,
141 ion availability can become a rate-limiting factor[45,46]. In each environment, *E. coli* were
142 firstly pre-cultured overnight in LB (at the appropriate salinity) and then for either 3 or 17 h in
143 fresh LB (or M9 medium at the same salinity, see below) for optimal growth or nutrient
144 depletion[47], respectively (see Methods).

145 Exposing *E. coli* to nutrient depletion alone (i.e. 17 h growth in 10 g/L NaCl LB),
146 favoured a steeper increase in intracellular 2-NBDG, compared to optimal growth conditions
147 (i.e. 3 h growth in 10 g/L NaCl LB) with a mean fluorescence of 417 and 250 a.u. after 300 s
148 incubation in 2-NBDG (Fig. 2b and 2a, respectively, ****, Table S2 and S3). However,
149 nutrient depletion alone did not significantly affect 2-NBDG accumulation at steady state with
150 a mean fluorescence of 740 and 733 a.u., respectively, at t=900 s (n.s., Table S2 and S3).

151 Exposing *E. coli* to salinity depletion alone (i.e. 3 h growth in 0.5 g/L NaCl LB), caused
152 a less steep intracellular 2-NBDG increase, compared to optimal growth conditions, with a
153 mean fluorescence of 148 and 250 a.u. after 300 s incubation in 2-NBDG (Fig. 2c and 2a,
154 respectively, ****, Table S2 and S3). Moreover, salt depletion also significantly reduced 2-
155 NBDG accumulation at steady state with a mean fluorescence of 373 and 733 a.u., respectively,
156 at t=900 s (****).

157 In striking contrast with the findings above, simultaneous exposure to nutritional and
158 salinity depletion (i.e. 17 h growth in 0.5 g/L NaCl LB) caused a steeper intracellular 2-NBDG
159 increase, compared to optimal growth conditions, with a mean fluorescence of 720 and 250
160 a.u. after 300 s incubation in 2-NBDG (Fig. 2d and 2a, respectively, ****, Table S2 and S3).
161 Moreover, combined nutrient and salt depletion also significantly enhanced 2-NBDG

accumulation at steady state with a mean fluorescence of 1714 and 733 a.u. at *t*=900 s, respectively (****, Table S2 and S3). These findings were further confirmed via separate flow cytometry measurements (red and black bars in Fig. S2, ****).

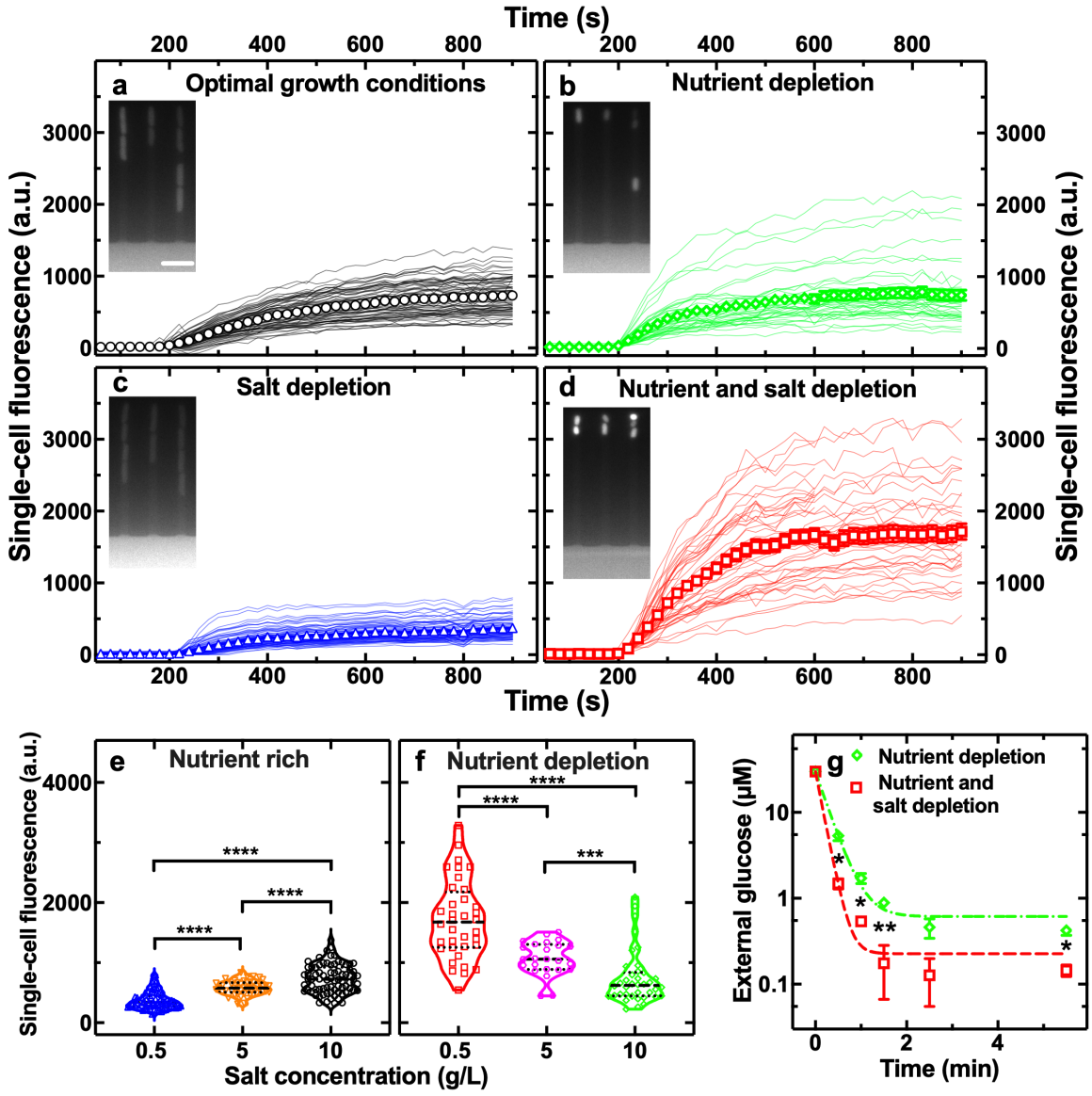

Figure 2. Glucose accumulation is greatest under combined nutritional and salinity depletion. Temporal dependence of the mean intracellular fluorescence of the glucose analogue 2-NBDG in individual *E. coli* under **a)** optimal growth conditions, **b)** nutrient depletion, **c)** salt depletion or **d)** combined nutrient and salt depletion. Lines are temporal dependences of the intracellular fluorescence of individual bacteria collated from biological triplicate. Symbols and error bars are the corresponding means and standard error of the means of such single-cell measurements. Noteworthy, we measured the 2-NBDG fluorescence as the mean fluorescent values of each pixel constituting each bacterium, thus normalizing by cell size. Coefficient of variations of these single-cell values and statistical tests of quantitative comparisons of values between different environments are reported in Table S2 and S3, respectively. Corresponding 2-NBDG intracellular fluorescence values during the removal of

extracellular 2-NBDG are reported in Fig. S5. Insets: corresponding fluorescence images at *t*=900s when the intracellular 2-NBDG accumulation has reached saturation levels in individual bacteria. Measurements were carried out on N=76, 38, 90 and 46 individual bacteria, in a)-d), respectively. Salinity-dependent distribution of single-cell fluorescence after 900 s incubation in 2-NBDG in **e)** nutrient-rich or **f)** nutrient-depleted environments. Dashed and dotted lines indicate the median and quartiles of each distribution, respectively. **g)** Temporal dependence of the extracellular glucose concentration for *E. coli* under nutrient (green diamonds) or nutrient and salt depletion (red squares). N=3 biological replicates for each environment. The dashed dotted and dashed lines are one phase exponential decay fittings to the data yielding a significantly smaller time constant *Tau* for *E. coli* under combined nutrient and salt depletion compared to nutrient depletion alone (*Tau* = (9±1) s vs (17±1) s, respectively, *). *: p-value<0.05, **: p-value<0.01, ***: p-value<0.001, ****: p-value<0.0001.

Moreover, we found that in nutrient-rich conditions 2-NBDG accumulation increased with salinity (Fig. 2e); on the other hand, under nutrient depletion 2-NBDG accumulation decreased with salinity (Fig. 2f). In fact, a 50% reduction in salinity (from 10 g/L down to 5 g/L NaCl) led to a 145% increase in 2-NBDG accumulation with a mean fluorescence of 740 and 1072 a.u. at *t*=900 s, respectively (***); a further 90% reduction in salinity (from 5 g/L down to 0.5 g/L NaCl, resembling the salinity change encountered during transition from the colon to the ileum[32]) led to a further 160% increase in 2-NBDG accumulation with a mean fluorescence of 1072 and 1714 a.u. at *t*=900 s, respectively (****). Taken together these data demonstrate that reducing the salinity content of the environment favours 2-NBDG accumulation in nutrient-poor but not in nutrient-rich environments.

Next, we verified that nutrient and salt depletion also synergistically boosts glucose accumulation (as a result of uptake and degradation), and not only the glucose analogue 2-NBDG. We performed plate reader based colorimetric assays on *E. coli* populations exposed to either nutrient, or simultaneous nutrient and salt depletion. We found that after 30 s incubation, the extracellular glucose concentration became significantly lower in *E. coli* that had been exposed to simultaneous nutrient and salt depletion compared to *E. coli* that had experienced nutrient depletion alone with a decay time constant *Tau* of (9.5±0.4) s and (16.7±1.2) s, respectively (*, red squares and green diamonds, respectively, in Fig. 2g). These

208 data therefore confirm that *E. coli* accumulate glucose significantly faster and to higher levels
209 after exposure to simultaneous nutrient and salt depletion compared to exposure to nutrient
210 depletion alone.

211 We further confirmed that the findings above were not affected by molecular leakage
212 through the cell membrane, cell integrity being essential for 2-NBDG uptake[5], by performing
213 separate experiments using thioflavin T (ThT). This compound stains intracellular
214 macromolecules[48,49] and is of comparable size to 2-NBDG. We found that, in contrast to 2-
215 NBDG, ThT accumulated to a significantly lesser extent in *E. coli* exposed to combined
216 nutritional and salinity depletion compared to optimal growth conditions (Fig. S3b and S3a,
217 red and black bars in Fig. S3c, respectively, and Table S4). Furthermore, *E. coli* exhibited
218 similar growth curves in both LB formulations (i.e. 0.5 g/L or 10 g/L NaCl). This data
219 confirmed that increased 2-NBDG accumulation under combined nutritional and salinity
220 depletion was not due to molecular leakage through compromised bacterial membranes and
221 that growth rate alone does not necessarily reflect important changes in bacterial
222 metabolism[50]. Finally, we sought to rule out the possibility that increased glucose
223 accumulation under combined nutritional and salinity depletion was a result of i) a nutritional
224 shift from LB to M9 (used for growth and 2-NBDG measurements, respectively), ii) low
225 abundance of divalent cations in LB medium or iii) changes in extracellular pH[45,51]. In order
226 to do so, we performed flow cytometry experiments on *E. coli* grown for 17 h in M9 with
227 limited (i.e. 0.1 g/L) glucose or ammonium (i.e. carbon or nitrogen limitation, respectively,[52]
228 see Methods) and either 0.5 or 10 g/L NaCl. Consistently with the data in Fig. 2, we found that
229 *E. coli* exposed to combined nutritional and salinity depletion in M9 accumulated 2-NBDG to
230 a significantly larger extent than *E. coli* exposed to nutritional depletion alone in M9 both with
231 glucose (mean fluorescence of 3007 and 1045 a.u. at t=900 s, red and green violins,
232 respectively, in Fig. S4a, ****) or ammonium as limiting factor (mean fluorescence of 3249

233 and 1776 a.u. at *t*=900 s, red and green violins, respectively, in Fig. S4b, ****). Furthermore,
234 the measured extracellular pH values were the same (8.0±0.1) for the nutrient depleted and
235 nutrient and salt depleted environments. Finally, *E. coli* displayed similarly large cell-to-cell
236 differences in the accumulation of 2-NBDG after pre-culturing in LB or M9 (coefficient of
237 variations of 38% and 60% after pre-culturing in 0.5 g/L or 10 g/L LB; coefficient of variations
238 of 66% and 69% after pre-culturing in 0.5 g/L or 10 g/L glucose-limited M9; coefficient of
239 variations of 43% and 64% after pre-culturing in 0.5 g/L or 10 g/L ammonia-limited M9).
240 Therefore, the observed heterogeneity in 2-NBDG accumulation was not driven by the
241 nutritional shift from LB to M9. Taken together this data demonstrate that when these two
242 environmental changes come together, they manifest a synergistic effect on intracellular
243 processes, such as glucose metabolism, that is greater than the effect of each environmental
244 change alone.
245

246 ***Glucose accumulation is heterogeneous under different environmental variations in a cell***
247 ***size-independent fashion***

248 Besides the above described different 2-NBDG accumulation traits across variant
249 environments, we also found substantial phenotypic heterogeneity within *E. coli* populations
250 in the same environment. This heterogeneity increased in the presence of nutrient or salt
251 depletion compared to optimal growth conditions (CV values of 2-NBDG intracellular
252 fluorescence in Table S2), suggesting specialization in metabolic functions to endure
253 environmental variations.

254 In order to gain a mechanistic understanding of these glucose accumulation traits in
255 variant environments, we firstly investigated the role played by cell area in 2-NBDG
256 accumulation. We studied the correlation of the total fluorescence of each bacterium at steady-
257 state (*t*=900 s) with the area of each bacterium. We found strong positive correlation between
258 single-cell area and total intracellular 2-NBDG fluorescence both via flow cytometry and via

microfluidics-microscopy (Fig. 3a and 3b, respectively, Pearson correlation coefficient larger than 0.7 in all tested environments).

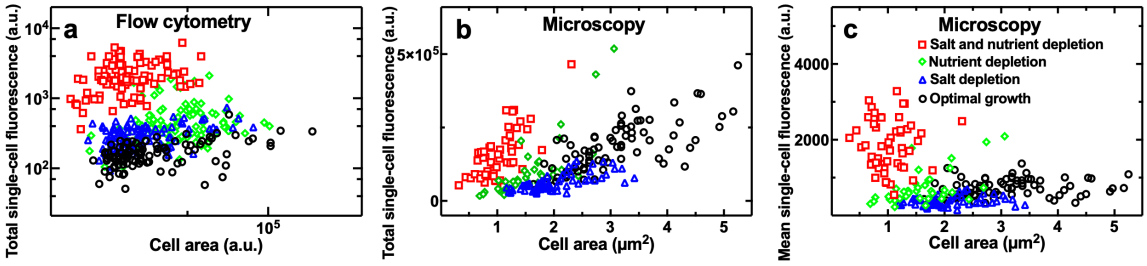

Figure 3. Glucose accumulation is heterogeneous across variant environments in a cell size-independent fashion. Size dependence of the total intracellular fluorescence of the glucose analogue 2-NBDG in individual *E. coli* under optimal growth conditions (circles), nutrient depletion (diamonds), salt depletion (triangles) or combined nutrient and salt depletion (squares) measured after 900s incubation in 2-NBDG via **a)** flow cytometry and **b)** microscopy in the mother machine. Pearson correlation coefficients of a) 0.35, 0.40, 0.42 and 0.32 and b) 0.71, 0.76, 0.69 and 0.71, respectively (all ****). **c)** Corresponding size dependence of the mean intracellular fluorescence normalized by cell size. Pearson correlation coefficients of 0.18 (ns), 0.57 (***), 0.16 (ns) and -0.01 (ns), respectively. ns=non significant, p-value>0.05; ***, p-value<0.001; ****, p-value<0.0001. N=100 representative measurements on individual bacteria in a) out of a total N=50000 measurements performed in biological triplicates. N>30 for each experimental condition collated from biological triplicates in b) and c).

However, when we calculated the mean 2-NBDG fluorescence for each bacterium, after normalizing by cell size[53], we found that, under combined nutritional and salinity depletion, *E. coli* exhibited significantly higher intracellular 2-NBDG fluorescence despite displaying significantly lower cell area compared to optimal growth conditions (squares and circles, respectively, in Fig. 3c). Moreover, we found a remarkable lack of correlation between the mean 2-NBDG fluorescence and cell size under optimal growth, salt depleted or nutrient and salt depleted conditions (Pearson correlation coefficients of 0.18 (ns), 0.16 (ns) and -0.01 (ns), respectively); we found instead a significantly positive correlation between 2-NBDG fluorescence and cell size under nutrient depletion (Pearson correlation coefficients of 0.57, ***). Finally, we still found substantial levels of heterogeneity in the mean 2-NBDG fluorescence values across the different environments (Fig. 3c). Taken together these data demonstrate that changes in cell size alone cannot account for the measured glucose

286 accumulation traits and heterogeneities in variant environments in contrast to the current
287 consensus[5,15].

288 ***Combined nutritional and salinity depletion boosts both glucose uptake and degradation***

289 We then sought to decouple the contribution of uptake and degradation mechanisms on the
290 measured 2-NBDG accumulation. To do this, we used a mathematical model describing 2-
291 NBDG accumulation in single bacteria using ordinary differential equation 1 (see Methods).
292 We inferred the uptake rate from the accumulation data in the presence of extracellular 2-
293 NBDG ($0<t<900$s, Fig. 2) and obtained an independent estimate of the degradation rate from
294 both the accumulation data in the presence of extracellular 2-NBDG ($0<t<900$s, Fig. 2) and the
295 degradation data in the absence of extracellular 2-NBDG ($t>1200$s, Fig. S5).

296 Nutritional depletion caused a significant decrease in 2-NBDG uptake rate but also a
297 significant increase in degradation rate compared to optimal growth conditions (Fig. 4a, 4d and
298 4e, Table S5). Moreover, both 2-NBDG uptake and degradation were more heterogeneous
299 under nutritional depletion (Table S6), further suggesting specialisation in metabolic functions
300 in stressed bacteria[44]. Finally, we did not find a significant correlation between uptake and
301 degradation rates at the single-bacterium level under nutritional depletion (Pearson correlation
302 coefficient of 0.27 compared to 0.42 for optimal growth conditions). This suggests that under
303 nutritional depletion, some bacteria specialize in fast uptake at the expense of reduced
304 degradation rates.

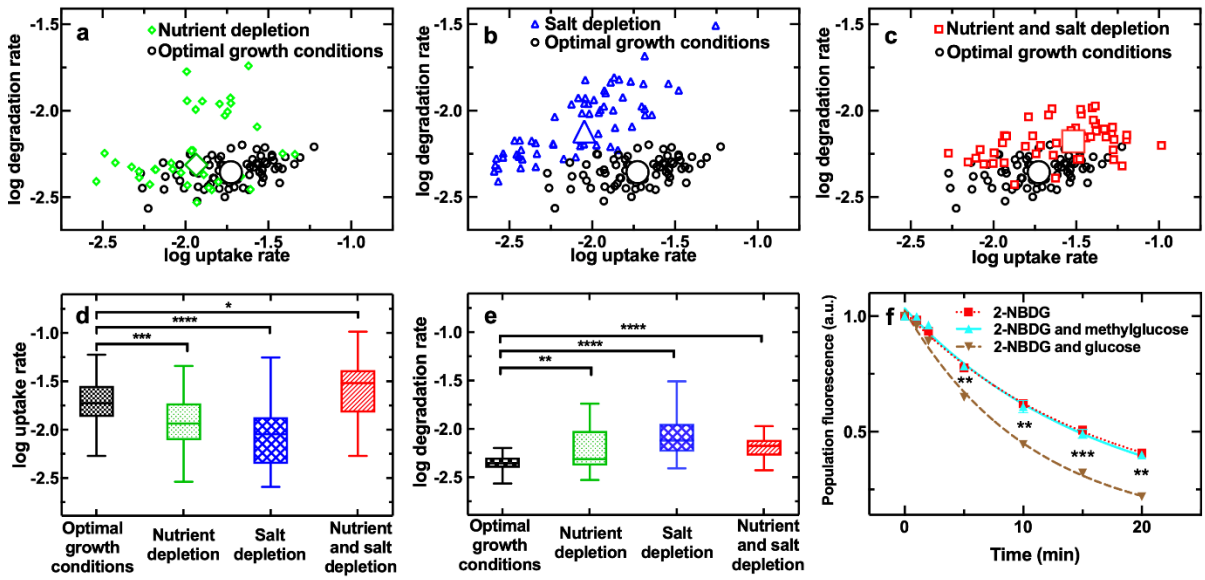

Figure 4. Combined nutritional and salinity depletion boosts both glucose uptake and degradation. a)-c) Single-cell correlation between the natural logarithm of 2-NBDG uptake rate and the natural logarithm of 2-NBDG degradation rate as predicted by Equation 1 for optimal growth conditions (circles), nutrient depletion (diamonds), salt depletion (triangles) or combined nutrient and salt depletion (squares), with Pearson correlation coefficients of 0.42 (***), 0.27 (ns), 0.80 (****) and 0.36 (*), respectively. N>30 for each experimental condition collated from biological triplicates, the large symbols are the medians of each set of single-cell values. Coefficient of variations of these single-cell values and statistical tests of quantitative comparisons of values between different environments are reported in Table S5 and S6, respectively. Corresponding distributions of **d)** natural logarithm of 2-NBDG uptake rate values and **e)** natural logarithm of 2-NBDG degradation rate values. The bottom and top of the box are the first and third quartiles, the band inside the box is the median, the bottom and top whiskers represent the 10th and 90th percentiles, respectively. **f)** Temporal dependence of the fluorescence of 2-NBDG when *E. coli* populations were incubated in 30 µM 2-NBDG alone (red squares), in the presence of 30 mM 3-O-methylglucose (cyan upward triangles), or in the presence of 30 mM glucose (brown downward triangles). N=3 biological replicates for each condition. The lines are one phase exponential decay fittings to the data yielding time constant *Tau* of (16.3 ± 1.1) min, (16.3 ± 1.2) min and (10.9 ± 0.5) min, respectively. *, p-value<0.05; ***, p-value<0.001; ****, p-value<0.0001.

Similarly, salinity depletion caused a significant decrease in 2-NBDG uptake rate but also a significant increase in degradation rate (Fig. 4b, 4d and 4e, Table S5). Furthermore, the CV of both uptake and degradation rate was higher under salinity depletion (Table S6). However, differently from nutritional depletion, salinity depletion favoured a strong positive correlation between uptake and degradation rates at the single bacterium level (Pearson

331 correlation coefficient of 0.80). This suggests that salt depletion favours the emergence of a
332 subset of the population specialising in both taking up and degrading 2-NBDG.

333 In contrast with the findings above, the combined presence of nutritional and salinity
334 depletion significantly increased both the uptake and degradation rate as well as intra-
335 population phenotypic heterogeneities in both parameters (Fig. 4c, 4d and 4e, Table S5 and
336 S6). This environment yielded a significant correlation between uptake and degradation rate
337 (Pearson correlation coefficient of 0.36). However, such correlation was weaker with respect
338 to that measured in the presence of salt depletion alone. This suggests that the additional
339 nutritional depletion favoured specialization in fast 2-NBDG uptake at the cost of reduced
340 degradation rates compared to champion degraders exposed to salinity depletion alone.

341 Next, we set out to confirm that the degradation of 2-NBDG by *E. coli* is linked to
342 activity of the bacterial glycolytic pathway, responsible for the degradation of glucose. We
343 investigated the degradation of the fluorescence of 2-NBDG in the presence of a competitive
344 and non-metabolizable inhibitor (i.e. 3-O-methyl glucose) or a competitive and metabolizable
345 inhibitor (i.e. glucose). The presence of a metabolizable inhibitor would stimulate bacterial
346 glycolytic activity and thereby enhance the 2-NBDG degradation, while the presence of a non-
347 metabolizable inhibitor would have no effect[5]. Accordingly, we found that the degradation
348 of the fluorescence of 2-NBDG in the presence of a competitive and metabolizable inhibitor
349 was significantly faster than the degradation of the fluorescence of 2-NBDG in the absence of
350 this inhibitor (brown downward triangles and red squares in Fig. 4f, respectively, time constant
351 *Tau* of (10.9 ± 0.5) min and (16.3 ± 1.1) min, respectively) since such inhibitor promotes
352 glycolytic activity. In contrast, we found that the degradation of the fluorescence of 2-NBDG
353 in the presence of a competitive and non-metabolizable inhibitor was comparable to the
354 degradation of the fluorescence of 2-NBDG in the absence of this inhibitor (cyan upward
355 triangles and red squares in Fig. 4f, respectively, time constant *Tau* of (16.3 ± 1.2) min and

356 (16.3 ± 1.1) min, respectively) since such inhibitor cannot be metabolized, thereby not
357 promoting the bacterial glycolytic activity. These data therefore demonstrate that 2-NBDG is
358 degraded as a consequence of the glycolytic pathway and can be used as a proxy for glucose
359 degradation.

360 Taken together these data demonstrate that simultaneous nutritional and salinity
361 depletion, that is the least favourable growth conditions investigated, has profound effects on
362 glucose metabolism, increasing both uptake and degradation rates at the level of the individual
363 bacterium, a synergistic effect that neither environmental changes alone can elicit.

364

365 ***Molecular mechanisms underpinning glucose accumulation traits under nutrient or salt***
366 ***depletion***
367

368 We then performed comparative transcriptomic and proteomic analysis between bulk
369 *E. coli* cultures in the four different environments investigated and measured the $\log_2$ fold
370 change in transcript or protein levels under nutrient or salt depletion compared to those
371 measured in optimal growth conditions. We then restricted our combined transcriptomic and
372 proteomic analysis to genes and proteins whose differential expression had a *p*-value adjusted
373 for false discovery rate smaller than 0.05[54]. We found a significant correlation between gene
374 and protein expression under salt depletion but no significant correlation under either nutrient
375 or nutrient and salt depletion (Fig. 5a, Pearson coefficient R = 0.13, 0.06 and 0.07, **, ns, ns,
376 respectively). We also found a stronger correlation between differential gene and protein
377 regulation under nutrient and nutrient and salt depletion compared to salt and nutrient and salt
378 depletion (Pearson coefficient R = 0.92 and 0.34, at the transcriptomic level and 0.89 and 0.45,
379 at the proteomic level, all ****).

380 To determine biological processes underlying acclimation of sugar metabolism to
381 changes in nutritional availability and environmental salinity, we clustered these combined

382 transcriptomic and proteomic data, identifying 13 distinct patterns of gene and protein
383 regulation (Fig. 5b and 5c, respectively, and Supplementary file 1).

384 Cellular biosynthetic processes (e.g. dicarboxylic acid, amide, organonitrogen and
385 peptide biosynthesis), gene expression and translation were significantly downregulated at the
386 transcriptomic and proteomic levels in both the nutrient depleted and the nutrient and salt
387 depleted environments compared to salt depletion alone (Clusters 5 and 9 in Fig. 5b and 5c,
388 ****).

389 Cell homeostasis biological processes including chemical, ion and cation homeostasis
390 were significantly upregulated under both nutrient and nutrient and salt depletion compared to
391 salt depletion alone or optimal growth conditions both at the transcriptomic and proteomic level
392 (Cluster 1 in Fig. 5b and 5c, **). Anaerobic respiration and polyol metabolic processes were
393 significantly upregulated under both nutrient and nutrient and salt depletion at the proteomic
394 level compared to salt depletion alone or optimal growth conditions (Cluster 13 in Fig. 5c, *)
395 in accordance with a previous report[55].

396 Crucially for this study, phosphoenolpyruvate-dependent sugar phosphotransferase
397 systems (PTS) were significantly upregulated at the proteomic level under both nutrient and
398 nutrient and salt depletion compared to salt depletion alone (Cluster 12 in Fig. 5c, **). These
399 proteins included the PTS system galacticol- and mannose-specific EIID components GatA
400 and ManZ, respectively, the latter transporting both mannose and glucose across the *E. coli*
401 inner membrane[13]. Furthermore, glucose metabolic processes were upregulated at the
402 proteomic level under nutrient or nutrient and salt depletion compared to salt depletion alone
403 (Cluster 12 in Figure 5c, **). These proteins included the formate acetyltransferase 1 PflB that
404 is involved in pyruvate fermentation (following glucose conversion to pyruvate) and formate
405 synthesis; the L-lactate dehydrogenase LldD which converts pyruvate to lactate; the glucose-
406 1-phosphatase Agp which converts glucose to glucose-1-phosphate; the putative glucose-6-

407 phosphate epimerase YeaD; as well as catabolic processes of other sugars such as galacticol

408 and deoxyribose.

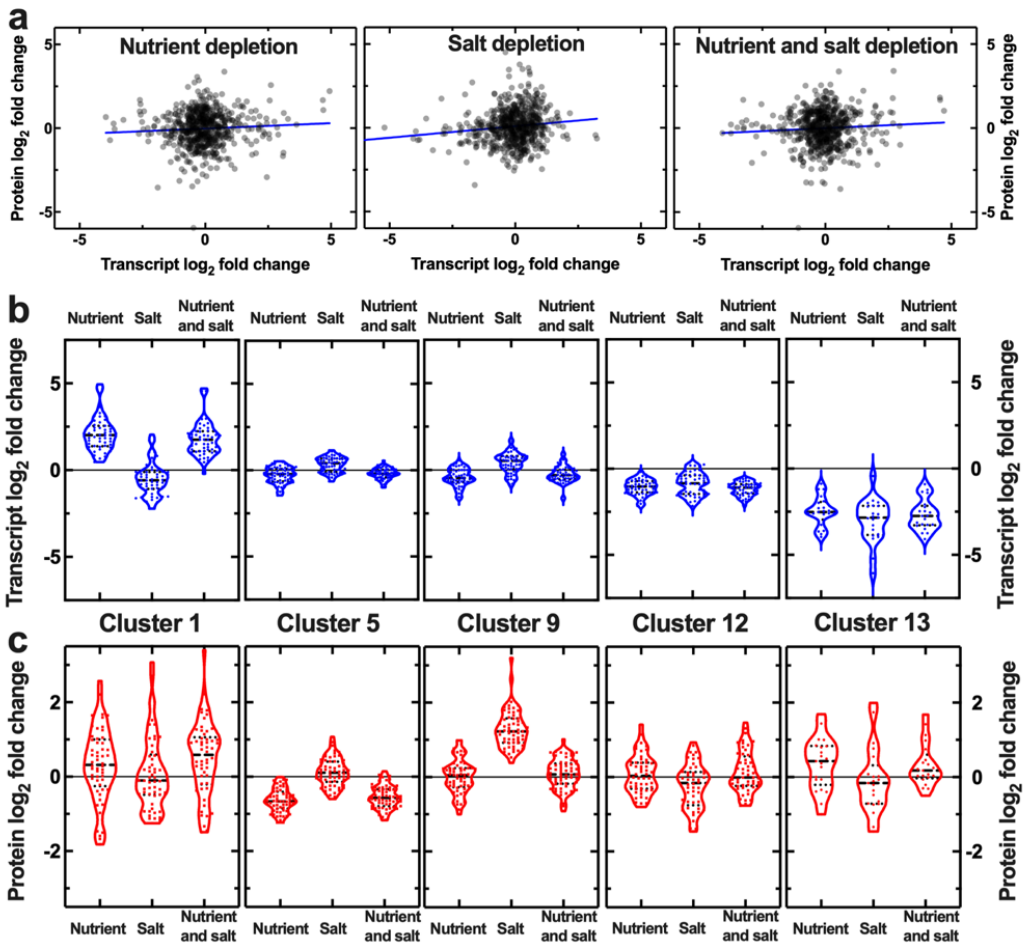

d

Cluster 1	Cluster 5	Cluster 9	Cluster 12	Cluster 13
cellular homeostasis	organonitrogen biosynthesis	amide biosynthesis	catabolic process	anaerobic respiration
chemical homeostasis	cellular biosynthesis	gene expression	organic catabolism	alditol metabolism
aldehyde metabolism	biosynthesis	translation	carbohydrate catabolism	polyol metabolism
homeostatic process	dicarboxylics biosynthesis	nitrogen biosynthesis	small molecule catabolism	cellular catabolism
ion homeostasis		peptide biosynthesis	response to DNA damage	
cation homeostasis		protein metabolism	PTS system	
inorganic ion homeostasis				

409

410 **Figure 5. Molecular mechanisms underpinning glucose accumulation traits under**
411 **nutrient or salt depletion. a)** Correlation between the $\log_2$ fold change in gene and protein
412 expression under nutrient, salt or nutrient and salt depletion. Each dot is the $\log_2$ fold change
413 in the number of copies for a single gene or protein, blue lines are linear regressions to the data
414 returning a Pearson correlation coefficient R=0.06, 0.13 and 0.07, (ns, ** and ns, respectively).
415 Transcript and protein reads were measured via RNA-sequencing and proteomics on samples
416 in biological triplicate and are reported in Supplementary files 2 and 3, respectively. Cluster

417 analysis of the combined transcriptomic and proteomic data above returned 13 clusters with
418 distinct patterns of **b)** gene and **c)** protein regulation under nutrient, salt or nutrient and salt
419 depletion. Each dot represents the $\log_2$ fold change in the number of copies for a single gene
420 or protein, dashed and dotted lines indicate the median and quartiles of each distribution,
421 respectively, the grey solid lines indicate a $\log_2$ fold change of zero. The lists of genes
422 belonging to each cluster are reported in Supplementary file 1. **d)** Biological processes
423 significantly over-represented in each of the clusters above. For clarity, only clusters displaying
424 significantly over-represented biological processes are reported in figure, data for the
425 remaining clusters are reported in Supplementary file 1.
426

427 To further validate these data, we performed clustering analysis on transcriptomic data
428 alone and found that carbohydrate transport and metabolic processes were significantly
429 downregulated under nutrient or nutrient and salt depletion compared to salt depletion alone or
430 optimal growth conditions (Clusters 8 and 12 in Supplementary file 2, ****). In striking
431 contrast, in our clustering analysis performed on proteomic data alone we found that
432 carbohydrate metabolic processes were significantly upregulated under nutrient or nutrient and
433 salt depletion compared to salt depletion alone or optimal growth conditions (Cluster 8 in
434 Supplementary file 3, ****). Besides the proteins found in Cluster 12 of our combined
435 transcriptomic-proteomic clustering analysis, Cluster 8 of the proteomic analysis included the
436 PTS system glucose-specific EIIA component Crr; the phosphocarrier protein PtsH; the
437 glucose-1-phosphate adenylyltransferase GlgC; the aconitate hydratase A AcnA; the enolase
438 Eno; the mannose-6-phosphate isomerase ManA; the phosphoglycerate kinase Pgk; the
439 pyruvate kinase PykF; the galactitol 1-phosphate 5-dehydrogenase GatD; the
440 phosphoglucomutase Pgm that is a highly conserved enzyme which functions at a key point in
441 glucose metabolism (the interconversion of glucose-1-phosphate and glucose-6-
442 phosphate,[56]), it is involved in several processes including bacterial pathogenesis[57] and
443 was previously found to be upregulated under nutrient depletion in minimal medium[55]. Here
444 we found that Pgm was further upregulated under combined nutrient and salt depletion
445 compared to nutrient or salt depletion alone ($\log_2$ fold change of 0.7, 0.4 and 0.3, respectively,
446 Supplementary file 3) in accordance with our data on glucose degradation rates (Fig. 4e). Taken

447 together these data demonstrate that under nutrient or combined nutrient and salt depletion
448 glucose uptake and degradation are regulated at translation rather than transcription level.
449 Moreover, when we carried out phosphoproteomics on *E. coli* cultured in the four
450 different environments above, we found that the phosphoglucomutase Pgm was one of the 13
451 proteins for which a phosphorylation event was detected (rows 8-9 in Supplementary file 4).
452 Other phosphorylated proteins included PpsA and GpmM involved in gluconeogenesis and
453 PpC and Icd (i.e. the first example of a protein phosphorylated on a serine or a threonine residue
454 in bacteria[55]) involved in the tricarboxylic acid cycle. We measured phosphorylation at two
455 different sites for the phosphopeptide GGPLADGIVITPSHNPPEDGGI that aligns with high
456 confidence to the Pgm amino acid sequence. The first phosphorylation event was recorded on
457 serine 13 of the phosphopeptide above with a site probability of 88% as defined by the
458 phosphoRS node of Proteome Discoverer software (i.e. serine 146 in the full protein sequence
459 in accordance with previous studies[55,58]). The amino acid residues surrounding this serine
460 are highly conserved in the phosphohexomutase superfamily to which Pgm belongs[59]. This
461 stretch of residues is known as the phosphoserine loop and is involved in the transfer of a
462 phosphoryl group from the serine residue above to glucose 6-phosphate to form a
463 biphosphorylated sugar intermediate. A high level of phosphorylation of this serine residue
464 increases Pgm flexibility and its enzymatic activity[59]. In accordance with our glucose
465 degradation data (Fig. 4e), we measured higher Pgm phosphorylation levels at serine 13 under
466 combined nutrient and salt depletion compared to optimal growth conditions (*, row 8 in
467 Supplementary file 4). This indicates that the combined nutrient and salt depletion drives a 12-
468 fold post-translational change as well as a 1.6-fold translational change in Pgm levels, thus
469 explaining the higher glucose degradation rate reported in Fig. 4. Moreover, we measured
470 significantly higher Pgm phosphorylation levels under combined nutrient and salt depletion
471 compared to optimal growth conditions (*, row 9 in Supplementary file 4) at a second site

472 within the phosphoserine loop. However, this site could not be defined with any degree of
473 confidence (i.e. site probability < 70%). Finally, a significantly higher degree of
474 phosphorylation under nutrient and salt depletion compared to optimal growth conditions was
475 also measured for the phosphoenolpyruvate synthase PpsA and the isocitrate dehydrogenase
476 Icd (* and **, rows 6 and 17 in Supplementary file 4) involved in gluconeogenesis and the
477 tricarboxylic acid cycle, respectively.

478 Considering the significant variations in Pgm both at the translational and post-
479 translational level, we set out to investigate the role played by Pgm in 2-NBDG accumulation.
480 To do this, we performed single-cell 2-NBDG accumulation measurements on both a Δ*pgm*
481 deletion mutant and the parental strain (PS). We found that under nutrient and salt depletion
482 the Δ*pgm* deletion mutant displayed significantly lower 2-NBDG accumulation compared to
483 the parental strain (purple hexagons and red squares in Fig. S6, respectively, ***). In contrast,
484 under optimal growth conditions the Δ*pgm* deletion mutant displayed 2-NBDG accumulation
485 comparable to the parental strain (magenta diamonds and black circles in Fig. S6, respectively,
486 ns). These data further confirm that modifications of Pgm at the translational and post-
487 translational level allow *E. coli* to enhance glucose accumulation.

488 Taken together these data demonstrate that simultaneous exposure to nutrient and salt
489 depletion decreases gene expression, translation and biosynthetic processes, while increasing
490 *E. coli* capability to take up and use glucose (and possibly other sugars) via variations at the
491 translational and post-translational level but not at the transcriptional level, thus corroborating
492 our glucose and 2-NBDG accumulation data presented in Fig. 2-4.

493

494 ***Glucose accumulation is not regulated by molecules secreted in the environment***

495 Finally, we also investigated the possibility that the combined nutritional and salinity depletion
496 caused bacterial secretion of molecules that affect intracellular 2-NBDG accumulation. These

497 molecules could include signalling secondary metabolites, such as putrescine and cadaverine,
498 that affect the functioning of membrane transporters[54]. In order to test this hypothesis, we
499 exposed *E. coli* grown in optimal growth conditions to the supernatant collected from *E. coli*
500 exposed to combined nutritional and salinity depletion. After 1h exposure to such supernatant,
501 we washed the microfluidic environment, introduced 30 μM 2-NBDG dissolved in glucose-
502 free M9 medium and measured 2-NBDG accumulation in individual bacteria. We then
503 compared these measurements to those performed without exposing bacteria to such
504 supernatant (squares and circles, respectively, in Fig. S7). In contrast to the hypothesis above,
505 we found that exposure to the supernatant collected from nutrient and salt depleted *E. coli* did
506 not enhance 2-NBDG accumulation. Taken together these data suggest that the metabolic
507 changes observed in the simultaneous nutritional and salinity depletion are not due to bacterial
508 secretion of compounds that can alter glucose metabolism.
509

510 **DISCUSSION**

511 Glucose uptake and utilization in bacteria have been previously linked to cell size, suggesting
512 that both glucose uptake and intracellular conversion are maximal in favourable growth
513 conditions, an idea that has led to the consensus that bacteria dwelling in stressful environments
514 reduce their metabolic capabilities[15–17,60]. However, these findings were obtained either in
515 optimal growth conditions or in the presence of only nutritional depletion[15]. In contrast, in
516 natural environments such as soil, aquatic systems or the human body, microbial communities
517 face multiple environmental changes[18,35]. Therefore, it is crucial to predict the effects of
518 multiple simultaneous environmental variations on the phenotypic diversity in microbial traits.
519 Here we demonstrate a hitherto unrecognised phenomenon in bacterial glucose
520 metabolism by finding enhanced glucose accumulation traits when *E. coli* are simultaneously
521 exposed to nutritional and salinity depletion. These traits are not displayed when bacteria are

522 exposed to either depletion alone, suggesting that the effect of these changes on glucose
523 metabolism is not additive[35]. In contrast with the general consensus, we show that these
524 differences in glucose accumulation traits cannot be explained by differences in cell size or
525 gene expression, a finding that needs to be taken into account when modelling metabolic fluxes
526 and when designing bioproduction in *E. coli*[14] since we show that increasing cell size does
527 not accelerate glucose metabolism.

528 We show instead that the measured metabolic changes are underpinned by variations
529 in glucose transport and metabolism at the translational and post-translational level. Protein
530 phosphorylation, especially on serine, threonine, or tyrosine, is one of the most common post-
531 translational modifications in bacteria[55]. Protein phosphorylation controls cell metabolism
532 and enhances cellular fitness under growth limiting conditions; for example, enzymes such as
533 phosphoglycerate mutase, phosphoglucomutase and adenosine 5′-phosphosulfate kinase
534 catalyse the turnover of phosphorylated sugars or metabolite phosphorylation by going through
535 a phosphorylated intermediate state during catalysis[61]. A previous study found a global
536 increase of protein phosphorylation levels under nutrient depletion[55]. Here we complement
537 this understanding by demonstrating elevated protein phosphorylation levels under nutrient
538 depletion, salt depletion or combined nutrient and salt depletion. Taken together these findings
539 point to a likely role of protein phosphorylation in variant environments. Indeed, we found
540 significantly higher phosphorylation levels of the phosphoglucomutase Pgm (at serine 146), a
541 highly conserved enzyme[59], under nutrient and salt depletion compared to optimal growth
542 conditions offering a mechanistic explanation of the measured glucose degradation rates.
543 Furthermore, Pgm was upregulated at the translational level under nutrient depletion in
544 accordance with a previous study using minimal medium[55], whereas we use LB medium,
545 further confirming that this metabolic response is not dictated by the pre-culturing medium.
546 We also found that Pgm was further upregulated under combined nutrient and salt depletion

547 compared to nutrient depletion alone corroborating our data on glucose degradation rates.
548 Finally, it is conceivable that other previously identified post-translational modifications (e.g.
549 the acetylation of GapA and FbaA[58], both involved in carbohydrate degradation) could
550 further contribute to the observed variations in glucose uptake and degradation rates.

551 We also showed that exposing *E. coli* growing in optimal conditions to the supernatant
552 collected from cells under nutrient and salt depletion did not enhance glucose accumulation
553 traits although this data should be corroborated in future via LC-MS metabolomics[62]. This
554 finding demonstrates that enhanced glucose accumulation traits are not driven by the impact of
555 physico-chemical properties of the nutrient and salt depleted environment on molecular
556 transport, but rather by continuous cellular adaptation to such an environment.

557 These data corroborate previous work about the impact of salinity on carbon uptake in
558 *Vibrio marinus* and cyanobacteria in natural environments[63,64], and on the remodelling of
559 *E. coli* glucose metabolism in the presence of environmental challenges[54,65]. Furthermore,
560 NaCl is routinely used in food products as an antimicrobial agent[66], therefore our findings
561 that adding NaCl decreases glucose accumulation in stationary phase bacteria should be taken
562 into account in both food preservation and bioproduction.

563 Our data also demonstrate, for the first time, that heterogeneity in glucose accumulation
564 traits under combined nutrient and salt depletion cannot be ascribed to cell-to-cell differences
565 in surface area alone neither can be ascribed to recovery from stationary phase[67]. In fact, we
566 measured similar levels of heterogeneity in glucose uptake and degradation in exponentially
567 growing and stationary phase *E. coli*. These data therefore suggest that cellular or
568 environmental parameters other than cell size underpin heterogeneity in glucose metabolism
569 adding to our current understanding of the relationship between cell growth rate and cellular
570 processes[68–72], including those preparing a cell for surviving fluctuations in environmental
571 conditions[73]. In this respect, we found that exposure to nutritional or salinity depletion

572 increases heterogeneity in both glucose uptake and degradation. This could be explained by the
573 recently reported heterogeneity in the expression of sugar metabolism genes[74,75]. Taken
574 together these data add new knowledge to the current understanding on phenotypic noise[76],
575 corroborating the view that cell-to-cell differences are ubiquitous within microbial
576 populations[67,76–78] and that there is substantial heterogeneity in the accumulation of
577 metabolites[5,44,74,75,79–84] or antimicrobials[40,85,86].

578 This newly introduced experimental approach could be applied to other fields of
579 research including medical mycology and crop protection, considering that glucose and its
580 fluorescent analogue 2-NBDG is taken up by pathogenic fungi such as *Candida albicans*[87].
581 The newly discovered glucose accumulation traits should be considered when investigating
582 cellular processes where salinity plays an important role such as cystic fibrosis associated lung
583 infections[34] and the enteropathogens present in the ileum and colon[32] . If confirmed for
584 microbes sampled from the environment, our findings will also inform modelling ecological
585 and evolutionary dynamics considering the extensive impact of climate change on the salinity
586 of freshwater ecosystems and naturally saline environments[25,30,35] which could
587 consequently lead to a profound effect on the capabilities of some species to take up and use
588 carbon sources.

589

590 **METHODS**

591 ***Strains, media and cell culture***

592 All chemicals were purchased from Merck unless otherwise specified. Lysogeny Broth (LB,
593 Melford) media made of 10 g/L Tryptone, 5 g/L Yeast extract and either 0.5, 5 or 10 g/L NaCl,
594 were used for culturing *E. coli*. Noteworthy, the 5 and 10 g/L NaCl LB formulation are
595 routinely used in microbiology, whereas the 0.5 g/L NaCl LB formulation is generally
596 employed only for selective cultivation with antibiotics that require low salt conditions. The

597 three formulations differ only in salt content, these do not differ in carbon and nitrogen source
598 content that it is known to affect glucose metabolism[62]. LB agar plates of respective NaCl
599 concentration with 15 g/L agar (Melford) were used for streak plates. Glucose-free M9-
600 minimal media, used to wash cells and dilute 2-(N-(7-Nitrobenz-2-oxa-1,3-diazol-4-
601 yl)Amino)-2-Deoxyglucose (2-NBDG) or Thioflavin T (ThT), was prepared using 5× M9
602 minimal salts (Merck), diluted as appropriate, with additional 2 mM $MgSO_4$, 0.1 mM $CaCl_2$, 3
603 μM thiamine HCl in milliQ water. Glucose or ammonia limited M9 media were prepared by
604 adding to this solution 0.1 g/L glucose or 0.1 g/L NH_4Cl, respectively[52], NaCl was added as
605 required at a final concentration of 0.5 g/L or 10 g/L, as appropriate. The parental strain *E. coli*
606 BW25113 and the single-gene knockout mutants Δ*pgm* were purchased from Dharmacon (GE
607 Healthcare) and stored in 50% glycerol stock at -80˚C. Streak plates for each strains were
608 produced by thawing a small aliquot of the corresponding glycerol stock every 2 weeks and
609 using LB agar containing either 0.5, 5 or 10 g/L NaCl. Exponentially growing cultures were
610 obtained by inoculating 100 mL of LB (or M9 medium) of 0.5, 5 or 10 g/L NaCl content with
611 100 μl of stationary phase liquid culture *E. coli* BW25113, then placed in a shaking incubator
612 at 200 rpm at 37˚C for 3 hours. Overnight cultures were prepared inoculating a single colony
613 of *E. coli* BW25113 in 200 mL of LB (or M9 medium) with 0.5, 5 or 10 g/L NaCl, then placed
614 in a shaking incubator at 200 rpm at 37˚C. Spent LB or M9 media used for resuspension of
615 prepared bacteria in microfluidic assays was prepared by centrifugation of overnight cultures
616 (4000 rpm, 20˚C, 10 min). The supernatant was then double filtered (Medical Millex-GS Filter,
617 0.22 μm, Millipore Corp) to remove bacterial debris from the solution as previously
618 reported[73]. 2-NBDG (Molecular weight=342 g/mol, ThermoFischer) was dissolved in
619 dimethyl sulfoxide (DMSO) at a stock concentration of 10mg/ml and stored at -20˚C.
620 ThT (Molecular weight=319 g/mol, Merck) was dissolved in milliQ water at a stock
621 concentration of 2 mM and stored at 4˚C.

622 ***Fabrication of microfluidic mother machine devices***

623 Microfluidic mother machine devices were fabricated in polydimethylsiloxane (PDMS,
624 Sylgard 184 silicone elastomer kit, Dow Corning) following previously reported
625 protocols[73,88]. A 10:1 (base:curing agent) PDMS mixture was cast on an epoxy mold of the
626 mother machine device provided by S. Jun[41]. Each mother machine device contains
627 approximately 6000 bacterial hosting channels with a width, height and length of 1, 1.5 and 25
628 μm, respectively. These channels are connected to a main microfluidic chamber with a width
629 and height of 25 and 100 μm, respectively. After degassing the PDMS mixture, this was
630 allowed to cure at 70˚C for 2 hours, before unmoulding the solid PDMS replica from the mother
631 machine epoxy mold. Using a 0.75 mm biopsy punch (RapidCore 0.75, Well-Tech) fluidic inlet
632 and outlet accesses were created at the two ends of the main chamber of the mother machine.
633 After ensuring accesses and surface of PDMS chip were completely clean using ethanol wash,
634 N_2 gas drying and removal of any small particles using adhesive tape (Scotch® Magic™ Tape,
635 3M), the PDMS chip, along with a glass coverslip (Borosilicate Glass No.1, Fisherbrand), were
636 further cleaned and surfaces hydrophilized using air plasma treatment (10 s exposure to 30 W
637 plasma power; Plasma etcher, Diener, Royal Oak, MI, USA) as previously reported[89]. Next,
638 PDMS and glass were brought in contact and irreversibly bonded. Upon bonding, the device
639 was placed for 5 min into an oven set at 70˚C to enhance the adhesion between the PDMS and
640 the glass surfaces. Finally, the device was filled with a 5 μL aliquot of 50 mg/ml bovine serum
641 albumin (BSA) in milliQ water and incubated at 37˚C for 1 hour; this step allowed to passivate
642 the charge within the channels post oxygen plasma treatment, thus screening any electrostatic
643 interaction between bacterial membranes and the glass and PDMS surfaces of the mother
644 machine.

645

646 ***Microfluidics-microscopy assay to measure 2-NBDG accumulation and degradation in***
647 ***individual E. coli bacteria***
648 The bacterial inoculum to be injected in the mother machine device was prepared via
649 centrifugation (5 min, 4000 rpm, 20˚C) of a 50 ml aliquot of an exponentially growing or
650 overnight culture (3 or 17 h after inoculation in LB or M9) and resuspended in spent LB (or
651 M9) medium (both prepared as described above) to an OD_{600} of 75. 50 mg/mL BSA was added
652 to the overnight culture before centrifugation to prevent bacterial cell aggregation[73]. The
653 bacterial suspension was then injected into the mother machine device and incubated at 37˚C
654 aiming to fill each bacterial hosting channel at an average density of one cell. Subsequently,
655 fluorinated ethylene propylene tubing (1/32" x 0.0008") was inserted into both inlet and outlet
656 accesses as previously reported[90]. A flow sensor unit (Flow Unit S, Fluigent, Paris, France)
657 was connected to the inlet tubing. This flow sensor unit was also connected to a pressure control
658 system (MFCS-4C, Fluigent), both being controlled via MAESFLO software (Fluigent)
659 allowing for computerised, accurate regulation of fluid flow into the microfluidic device. The
660 above described spent LB medium was used to clear the main channel of excess bacteria that
661 had not entered the bacterial hosting channels, initially flowing at 300 µL/h for 8 min and then
662 set to a flow rate of 100 µL/h. The loaded microfluidic device was mounted onto an inverted
663 microscope (IX73 Olympus, Tokyo, Japan) following the flushing of the main channel with
664 spent media and centred on one area of the mother machine containing 46 of the 6000 bacteria
665 hosting channels; after visual inspection of the device, using automated stages for both coarse
666 and fine movements (M-545.USC and P-545.3C7, Physik Instrumente, Karlsruhe, Germany),
667 this area was selected on account of it containing the highest number of channels filled with
668 one bacterium. Initial bright-field and fluorescence images were acquired using a 60×, 1.2 N.A.
669 objective (UPLSAPO60XW, Olympus) and a sCMOS camera (Zyla 4.2, Andor, Belfast, UK),
670 and, for the fluorescence image only, a FITC filter and exposure to blue LED illumination at

671 15% of its maximum power (200mW, CoolLED pE-300white, Andover, UK) for 0.1 s.
672 Following this, 30 μM 2-NBDG in M9-minimal medium was introduced into the microfluidic
673 device at an initial flow rate of 300 μL/h for 8 min, then 100 μL/h thereafter. Simultaneously,
674 a fluorescence image was acquired every 20 s for a period of 900 s using the settings described
675 above, a custom built LabView software and a 7-way Multi I/O timing cable (Andor, Belfast,
676 UK) ensuring the LED only illuminated during image acquisition, thus reducing
677 photobleaching. This same protocol was also employed to investigate the accumulation of 50
678 μM ThT in M9-minimal medium in individual *E. coli* bacteria.
679 At *t*=1200 s, the 2-NBDG solution was flushed away and exchanged to fresh LB or M9 medium
680 (of appropriate NaCl concentration) flowing at an initial flow rate of 300 μl/h for 8 min, then
681 100 μl/h thereafter. This step allowed monitoring the degradation of 2-NBDG that had
682 accumulated in each individual bacterium by acquiring a fluorescence image every 20 s until
683 *t*=2100 s.
684
685 ***Flow cytometry measurements***
686 *E. coli* cultures were prepared as described above and 1 mL aliquoted into an Eppendorf at *t*=3
687 or 17 h and spun down at 13,400 rpm for 5 min using a microcentrifuge (SLS Lab Basics, UK).
688 For uptake experiments, the bacterial pellet was resuspended in 1 mL of fluorescent substrate
689 solution; either 30 μM 2-NBDG or 50 μM ThT and incubated for 15 or 45 min, respectively.
690 After incubation, cells were pelleted at 13,400 rpm for 5 min using a table top centrifuge and
691 resuspended in 1 ml of phosphate buffer solution (PBS) and further diluted as necessary.
692 Measurements were then performed using a Beckman Coulter CytoFLEX S (Beckman Coulter,
693 United States) and cell fluorescence quantified using the fluorescein isothiocyanate (FITC)
694 channel (488 nm excitation and 525/40 nm band-pass filter), with PMT voltages of FSC 1000,
695 SSC 500, FITC 250 and a threshold value of 10000 for SSC-A to exclude any background

696 noise. These measurements were not normalized by cell size. Data were initially collected using
697 CytExpert software, exported and later processed using GraphPad Prism 9. For degradation
698 assays in the presence of competitive inhibitors, the bacterial pellet was resuspended in 30 µM
699 2-NBDG and incubated for 15 min as for the uptake experiments above. Following this 15-min
700 incubation, 1 mL of D-glucose (metabolizable inhibitor) or 3-O-methylglucose (non-
701 metabolizable inhibitor) was added to the sample at a final concentration of 30 mM. Samples
702 were then diluted as necessary in PBS and measured via flow cytometry at intervals over 20
703 min as described above.
704
705 ***Glucose colorimetric assay***
706 17-hour stationary phase cultures grown in 0.5 g/L (nutrient and salt depletion) or 10 g/L NaCl
707 LB (nutrient depletion) were prepared (as described above) in biological triplicate, reaching an
708 optical density at 600 nm of 5 in both conditions. 1 mL of each culture was centrifuged at
709 13,400 rpm for 5 min using a microcentrifuge. Each pellet was subsequently resuspended in 1
710 mL 30 µM D-glucose and incubated for different time intervals. Following incubation,
711 centrifugation was carried out as above but at 0°C, to reduce any further glucose uptake by
712 cells. The supernatant of each sample was collected while the pellet was discarded. Using a
713 glucose assay kit (Sigma Aldrich, Montana, United States), 50 µL of each supernatant sample
714 was added to 50 µL master reaction mix (46 µL glucose assay buffer, 2 µL glucose probe and
715 2 µL glucose enzyme mix) and incubated in the dark at room temperature for 15 min.
716 Oxidisation of any glucose present in the sample occurred during incubation, thus generating
717 a colorimetric product, the absorbance of which was measured at 570 nm using a CLARIOstar
718 PLUS plate reader (BMG Labtech, UK). For each experimental repeat, glucose standards were
719 obtained by performing a serial dilution between 0 and 10 µL of a 1 nmole/µL glucose standard
720 solution added to 50 µl of the master reaction mix above, brought to 100 µL per well with

721 glucose assay buffer as needed. Absorbances collected for glucose standard wells were then
722 used as a standard curve by which sample absorbances were compared and interpolated.
723 To calculate the concentration of glucose present in each sample, background absorbance
724 (assay blank of standard curve where 0 µl of glucose standard solution was present in the
725 sample) was first subtracted and then the following equation was used:

726 $$C = \frac{S_a}{S_v}$$

727 Where S_a is the amount of glucose in the unknown sample (in nmole) from standard curve, S_v
728 is the sample volume (µL) added into the well and C describes the concentration of glucose in
729 the sample.
730

731 ***Image and data analysis***

732 Images were processed using ImageJ software as previously described[88,91] tracking each
733 individual bacterium throughout their incubation in and removal of 2-NBDG. A rectangle was
734 drawn around each bacterium at every time point, obtaining its width, length and mean
735 fluorescence intensity. The mean fluorescence intensity for each bacterium was normalised by
736 cell size, to account for cell cycle related variations in glucose accumulation[53]. The
737 background fluorescence (i.e. the fluorescence of extracellular 2-NBDG) at each time point
738 was measured for each bacterium as follow as follows: a rectangle, of similar dimensions to
739 those drawn around the bacteria, was drawn and positioned, at the same distance from the main
740 channel, in the nearest channel that did not contain bacteria and the mean fluorescence value
741 within this rectangle was extracted via ImageJ. This background fluorescence was subtracted
742 from the corresponding bacterium's fluorescence value at every time point as previously
743 reported[73].
744 These fluorescence data were then analysed and plotted using GraphPad Prism 9. Statistical
745 significance was tested using unpaired, two-tailed, Welch's *t*-test unless specified otherwise.

746 Error bars displayed in all graphs represent the standard error of the mean (SEM), however,
747 due to the large sample sizes, error bars in some figures are small compared to the
748 corresponding mean values and thus hidden behind data points. Pearson correlation, medians
749 and coefficient of variations were also calculated using GraphPad Prism 9.
750
751 ***Transcriptomic analysis***
752 RNA isolation, library preparation, sequencing, and transcriptomic data processing was
753 performed as previously reported[54,92]. Briefly, *E. coli* cultures in high or low salt
754 exponential (optimal growth conditions or salt depletion, respectively) and stationary phase
755 (nutrient depletion or nutrient and salt depletion, respectively) were prepared as described
756 above and 500 µL aliquots were taken from each culture after t=3 and 17 h after inoculation in
757 LB, respectively, in biological triplicate for each of the four environmental conditions.
758 RNAprotect Bacteria Reagent (Qiagen) was added to each aliquot. Extractions were performed
759 using RNeasy Mini Kit (Qiagen) for exponential phase aliquots and RNeasy Micro Kit
760 (Qiagen) for stationary phase aliquots following manufacturer instructions and previously
761 reported protocols[54,92]. DNA removal during extraction was carried out by using RNase-
762 Free DNase I (Qiagen). RNA concentration and quality were measured using Qubit 1.0
763 fluorometer (ThermoFisher Scientific) and 2200 TapeStation (Agilent), respectively, and only
764 samples with an RNA integrity number larger than 8 were taken forward. Transcript abundance
765 was quantified using Salmon for each gene in all samples. Subsequent differential analysis was
766 performed using DEseq2 in R software to quantify the $\log_2$ fold change in transcript reads[93]
767 for each gene in aliquots under nutritional, salinity or combined nutritional and salinity
768 depletion each compared to growth in optimal conditions. Significantly differentially expressed
769 genes were defined as having a $\log_2$ fold change with respect to optimal growth conditions
770 greater than 1 and a p-value adjusted for false discovery rate of <0.05[24].

771 ***Proteomic Analysis***

772 *E. coli* whole cell preparation was performed using 1.5 L cultures as described above. At 3 and
773 17 h, for exponential and stationary phase respectively, each culture was centrifuged at 4700
774 rpm ThermoFisher, USA) at 4°C for 20 min. Pellets were then resuspended in 5 mL of lysis
775 buffer (20 mM Tris-HCl (pH 8.0), 0.5 M NaCl). Subsequently, one cOmplete™, EDTA-free
776 Protease Inhibitor Cocktail (Roche, Sigma Aldrich) tablet and one phosSTOP™ (Roche, Sigma
777 Aldrich) tablet were added to each sample. Sonication cycles for complete cell lysis were
778 performed at 70% amplitude in a Sonics Vibracell VC-505 instrument (Sonics and Materials
779 Inc., Newton, CT, USA) on ice. Lysate was then centrifuged to remove cell debris at 14400
780 rpm 4°C for 30 min and pellet was discarded. Aliquots of 80 µg of each sample were digested
781 with trypsin (2.5 µg trypsin per 100 µg protein; 37°C, overnight), labelled with Tandem Mass
782 Tag (TMT) eleven plex reagents according to the manufacturer's protocol (Thermo Fisher
783 Scientific) and the labelled samples pooled.

784 For the Total proteome analysis, an aliquot of 50 µg of the pooled sample was desalted using
785 a SepPak cartridge according to the manufacturer's instructions (Waters, Milford,
786 Massachusetts, USA). Eluate from the SepPak cartridge was evaporated to dryness and
787 resuspended in buffer A (20 mM ammonium hydroxide, pH 10) prior to fractionation by high
788 pH reversed-phase chromatography using an Ultimate 3000 liquid chromatography system
789 (Thermo Fisher Scientific). In brief, the sample was loaded onto an XBridge BEH C18 Column
790 (130 Å, 3.5 µm, 2.1 mm × 150 mm, Waters, UK) in buffer A and peptides eluted with an
791 increasing gradient of buffer B (20 mM Ammonium Hydroxide in acetonitrile, pH 10) from 0-
792 95% over 60 min. The resulting fractions (5 in total) were evaporated to dryness and
793 resuspended in 1% formic acid prior to analysis by nano-liquid chromatography tandem mass
794 spectrometry (LC MSMS) using an Orbitrap Fusion Lumos mass spectrometer (Thermo
795 Scientific).

796 For the Phospho proteome analysis, the remainder of the TMT-labelled pooled sample was also
797 desalted using a SepPak cartridge (Waters, Milford, Massachusetts, USA). Eluate from the
798 SepPak cartridge was evaporated to dryness and subjected to TiO_2-based phosphopeptide
799 enrichment according to the manufacturer's instructions (Pierce). The flow-through and
800 washes from the TiO_2-based enrichment were then subjected to FeNTA-based phosphopeptide
801 enrichment according to the manufacturer's instructions (Pierce). The phospho-enriched
802 samples were again evaporated to dryness and then resuspended in 1% formic acid prior to
803 analysis by nano-LC MSMS using an Orbitrap Fusion Lumos mass spectrometer (Thermo
804 Scientific).
805 High pH RP fractions (Total proteome analysis) or the phospho-enriched fractions (Phospho-
806 proteome analysis) were further fractionated using an Ultimate 3000 nano-LC system in line
807 with an Orbitrap Fusion Lumos mass spectrometer (Thermo Scientific). In brief, peptides in
808 1% (vol/vol) formic acid were injected onto an Acclaim PepMap C18 nano-trap column
809 (Thermo Scientific). After washing with 0.5% (vol/vol) acetonitrile 0.1% (vol/vol) formic acid,
810 peptides were resolved on a 250 mm × 75 µm Acclaim PepMap C18 reverse phase analytical
811 column (Thermo Scientific) over a 150 min organic gradient, using 7 gradient segments (1-
812 6% solvent B over 1 min, 6-15% B over 58 min, 15-32%B over 58 min, 32-40%B over 5 min,
813 40-90%B over 1 min, held at 90%B for 6 min and then reduced to 1%B over 1 min) with a
814 flow rate of 300 nL/min. Solvent A was 0.1% formic acid and Solvent B was aqueous 80%
815 acetonitrile in 0.1% formic acid. Peptides were ionized by nano-electrospray ionization at 2.0
816 kV using a stainless-steel emitter with an internal diameter of 30 µm (Thermo Scientific) and
817 a capillary temperature of 300°C.
818 All spectra were acquired using an Orbitrap Fusion Lumos mass spectrometer controlled by
819 Xcalibur 3.0 software (Thermo Scientific) and operated in data-dependent acquisition mode
820 using an SPS-MS3 workflow. Fourier-transformed mass-spectrometry 1 (FTMS1) spectra were

821 collected at a resolution of 120,000, with an automatic gain control (AGC) target of 200,000
822 and a maximum injection time of 50 ms. Precursors were filtered with an intensity threshold
823 of 5,000 according to charge state (to include charge states 2-7) and with monoisotopic peak
824 determination set to Peptide. Previously interrogated precursors were excluded using a
825 dynamic window (60 s +/-10 ppm). The MS2 precursors were isolated with a quadrupole
826 isolation window of 0.7m/z. Ion trap mass-spectrometry (ITMS2) spectra were collected with
827 an AGC target of 10 000, max injection time of 70ms and Collision induced dissociation (CID)
828 energy of 35%.
829 For FTMS3 analysis, the Orbitrap was operated at 50,000 resolution with an AGC target of
830 50,000 and a maximum injection time of 105 ms. Precursors were fragmented by high energy
831 collision dissociation (HCD) at a normalised collision energy of 60% to ensure maximal TMT
832 reporter ion yield. Synchronous Precursor Selection (SPS) was enabled to include up to 10
833 MS2 fragment ions in the FTMS3 scan.
834 The raw data files were processed and quantified using Proteome Discoverer software v2.1
835 (Thermo Scientific) and searched against the UniProt *Escherichia coli* (strain K12) [83333]
836 database (downloaded November 2020: 8061 entries) using the SEQUEST HT algorithm.
837 Peptide precursor mass tolerance was set at 10 ppm, and MS/MS tolerance was set at 0.6 Da.
838 Search criteria included oxidation of methionine (+15.9949) as a variable modification and
839 carbamidomethylation of cysteine (+57.0214) and the addition of the TMT mass tag
840 (+229.163) to peptide N-termini and lysine as fixed modifications. For the Phospho-proteome
841 analysis, phosphorylation of serine, threonine, tyrosine, histidine and aspartic acid (+79.966)
842 was also included as a variable modification. Searches were performed with full tryptic
843 digestion and a maximum of 2 missed cleavages were allowed. The reverse database search
844 option was enabled and all data was filtered to satisfy false discovery rate (FDR) of 5%.
845 Protein differential abundance analysis was carried out using *limma*[94], which has been shown

846 to be appropriate for proteomics data[95]. *p*-values were adjusted for false discovery rate using
847 the method of Benjamini and Hochberg[96].
848
849 ***Cluster and gene ontology analysis***
850 Clustering analysis was performed using the mclust package (version 5.4.7) for R[97].
851 Clustering was performed on the transcriptomic and proteomic $\log_2$ fold-change data separately
852 and then simultaneously on both data sets. Hyperspherical models of equal and unequal volume
853 were tested for a range of 2 to 20 clusters and the minimal, best-fitting model was identified
854 by the Bayes information criterion. We observed generally larger fold-change magnitudes in
855 the transcriptomic data, which may dominate in simultaneous clustering on both data sets.
856 Therefore, prior to simultaneous clustering of proteomic and transcriptomic data, the fold-
857 changes for each condition within each 'omics data set were standardized by dividing by the
858 sample standard deviations.

859 Gene Ontology enrichment analysis was performed using the clusterProfiler package (version
860 3.16.1) for R[98]. Enrichment in terms belonging to the "Biological Process" ontology was
861 calculated for each gene cluster, relative to the set of all genes quantified in the experiment, via
862 a one-sided Fisher exact test (hypergeometric test). *P* values were adjusted for false discovery
863 by using the method of Benjamini and Hochberg[96]. Finally, the lists of significantly enriched
864 terms were simplified to remove redundant terms, as assessed via their semantic similarity to
865 other enriched terms, using clusterProfiler's simplify function.

866
867 ***Mathematical model and parameter inference***
868 In order to rationalise the data acquired via our microfluidics-microscopy assay, we described
869 the dynamics of intracellular 2-NBDG concentration in single cells using the following
870 ordinary differential equation (ODE):

871 $$\frac{d[gluc]_{in}}{dt} = -d_{gluc}\,[gluc]_{in} + \frac{u_{gluc}}{V_c}\,[gluc]_{ex}.$$

872 This equation describes the change of intracellular 2-NBDG concentration, $[gluc]_{in}$, over time
873 (left hand-side term) as the sum of two processes: intracellular 2-NBDG degradation (negative
874 term in the right hand-side) occurring at rate $d_{gluc}\,[gluc]_{in}$, and 2-NBDG uptake (positive
875 term in the right hand-side) that we model as a first-order kinetics occurring at rate
876 $\frac{u_{gluc}}{V_c}\,[gluc]_{ex}$, similarly to previous models[5]. Furthermore, $[gluc]_{ex}$ denotes the time-varying,
877 extracellular 2-NBDG concentration. Here, since we measure the fluorescent intensity in the
878 bacterial hosting channels (dashed line in Fig. 1) we chose to solve the ODE numerically
879 approximating $[gluc]_{ex}$ at all times as a piecewise linear function. We note that with any
880 functional form of $[gluc]_{ex}$ the ODE admits to an analytical solution, however the complex
881 structure of the solution (involving time integration) defeats the purpose of using this directly
882 for inference. An alternative approach would have been to assume instantaneous changes of
883 external 2-NBDG at times $t = 0$ (addition) and $t = t_1 = 1{,}200s$ (removal) and use the
884 following simple analytical solution for inference purposes:

885 $$[gluc]_{in} = \begin{cases} \frac{u_{gluc}[gluc]_{ex}}{d_{gluc}V_c}\left(1 - e^{-d_{gluc}t}\right), & t_1 \geq t \geq 0 \\ \frac{u_{gluc}[gluc]_{ex}}{d_{gluc}V_c}\left(e^{-d_{gluc}(t-t_1)} - e^{-d_{gluc}t}\right), & t \geq t_1 \end{cases}$$

886 However, such an approach misses out information (i.e. non-instantaneous 2-NBDG delivery)
887 that is crucial for providing an accurate description of the kinetics in 2-NBDG accumulation in
888 single cells. Rate constant u_{gluc} ($\mu\mathrm{m}^3\mathrm{s}^{-1}$) and d_{gluc} (s^{-1}) dictate the rate of 2-NBDG uptake,
889 and degradation, respectively. Parameter V_c ($\mu\mathrm{m}^3$) denotes the cellular volume, and its
890 presence in the denominator of the uptake rate term ensures that intracellular 2-NBDG
891 concertation is reduced in cells with larger volumes due to dilution (other parameters being the
892 same). We estimate V_c using the measured width and length of each cell and assuming a rod-

like shape. We use the model and Bayesian inference techniques to extract information regarding rate parameters u_{gluc}, d_{gluc} from our single-cell measurements of intracellular 2-NBDG accumulation and degradation. To capture cell-to-cell heterogeneity we employ a hierarchical Bayes approach where parameters u_{gluc} and d_{gluc} vary between single cells according to an underlying population distribution. To model this unknown population distribution we use an infinite Gaussian mixture model (iGMM)[99], which being a non-parametric Bayesian model offers greater modelling flexibility than standard parametric distributional models. We note that the hierarchical Bayes approach also allow us to naturally incorporate in the model uncertainty (or lack of information) regarding the prior distribution of u_{gluc} and d_{gluc}, as we do not have to specify explicit priors for these parameters but instead specify priors for the hyper-parameters of the iGMM model. Choices of priors for the iGMM hyper-parameters are given in Table 1. To sample from the posterior distribution of the two parameters, $u_{gluc,i}$ and $d_{gluc,i}$, for each cell i, we employed an iterative Gibbs sampling scheme. Each iteration of the sampling scheme, indexed by k, consists of two steps. In the first step, parameters $a_{gluc,i}^{(k)}$ and $d_{gluc,i}^{(k)}$ are sampled for each cell (indexed by i) given the data, $\boldsymbol{y}_i = \{y_{i,t}: i = 1, \dots, M, t = 1, \dots, Z\}$, cellular volume $V_{c,i}$, external 2-NBDG profile $[gluc]_{ex,i}$, coefficient of variation of the measurement error CV_{error}, and the iGMM parameterisation from the previous iteration, $\boldsymbol{\theta}_{iGMM}^{(k-1)}$. In the second step, iGMM parameters, $\boldsymbol{\theta}_{iGMM}^{(k)}$, are sampled anew given the current values of $a_{gluc,i}^{(k)}$ and $d_{gluc,i}^{(k)}$. In summary, the algorithm involves sampling iteratively from the following target distributions:

a) $a_{gluc,i}^{(k)}, v_{gluc,i}^{(k)} \sim P\left(\cdot \,|\boldsymbol{\theta}_{iGMM}^{(k-1)}, \boldsymbol{y}_i, V_{c,i}, [gluc]_{ex,i}, CV_{error}\right)$ for each cell i;

b) $\boldsymbol{\theta}_{iGMM}^{(k)} \sim P\left(\cdot \,|a_{gluc,i}^{(k)}, v_{gluc,i}^{(k)}\right)$.

To sample parameters $u_{gluc,i}$ and $d_{gluc,i}$ in step a) we assume that the 2-NBDG accumulation and degradation measurement, $y_{i,t}$, taken form cell i at time-point t obeys a gaussian

distribution, $y_{i,t} \sim \mathcal{N}([gluc]_{i,t}, \sigma_{i,t})$, with mean $[gluc]_{i,t}$ and standard deviation $\sigma_{i,t} = CV_{error} \cdot [gluc]_{i,t}$. Here $[gluc]_{i,t}$ is obtained by solving the model numerically using the corresponding rate parameters, cellular volume, and external 2-NBDG concertation profile. This assumption allows us to use a single step of the Metropolis-Hastings algorithm to draw samples from the target distribution since this is proportional to a product of densities (gaussians and mixture of gaussians) all of which can be straightforwardly evaluated, i.e.,

$$P\left(a_{gluc,i}^{(k)}, v_{gluc,i}^{(k)} | \boldsymbol{\theta}_{iGMM}^{(k-1)}, \boldsymbol{y}_i, V_{c,i}, [gluc]_{ex,i}, CV_{error}\right) \propto$$

$$P\left(\boldsymbol{y}_i | a_{gluc,i}^{(k)}, v_{gluc,i}^{(k)}, V_{c,i}, [gluc]_{ex,i}, CV_{error}\right) P\left(a_{gluc,i}^{(k)}, v_{gluc,i}^{(k)} \middle| \boldsymbol{\theta}_{iGMM}^{(k-1)}\right) =$$

$$\left[\prod_t P\left(y_{i,t} | a_{gluc,i}^{(k)}, v_{gluc,i}^{(k)}, V_{c,i}, [gluc]_{ex,i}, CV_{error}\right)\right] P\left(a_{gluc,i}^{(k)}, v_{gluc,i}^{(k)} \middle| \boldsymbol{\theta}_{iGMM}^{(k-1)}\right) =$$

$$\left[\prod_t \mathcal{N}([gluc]_{i,t}, \sigma_{i,t})\right] P\left(a_{gluc,i}^{(k)}, v_{gluc,i}^{(k)} \middle| \boldsymbol{\theta}_{iGMM}^{(k-1)}\right).$$

In step b) of the algorithm, we sampled from the target distribution using the algorithm as proposed by Rasmussen[99]. In the first iteration of the scheme, $k = 1$, we initialise $u_{gluc,i}^{(1)}, d_{gluc,i}^{(1)}$ to values obtained using maximum likelihood estimation (perfomed using Matlab's in-built nonlinear least-squares solver lsqcurvefit; using the Levenberg-Marquardt optimization algorithm and with the maximum number of iterations set to 15). The scheme was implemented and run using Matlab R2018.

Hyper-parameters	Hyper parameter description	Prior
α	Concentration parameter of the Dirichlet prior.	$\alpha \sim Gamma(1,1)$
λ	Mean of the 2D-Guassian prior for component means	$\lambda \sim Normal(\mu_\vartheta, \Sigma_\vartheta)$

r^{-1}	St. deviation of the 2D-Guassian prior for component means.	$r \sim Wishart(\Sigma_{\vartheta}^{-1}/2,2)$
$2\,\beta$	Shape parameter of the 2D Wishart prior for component precisions (ie, inverse st. devs.)	$\beta - 1 \sim Gamma(1,1)$
$w^{-1}/2$	Scale matrix of the 2D Wishart prior for component precisions (ie, inverse st. devs.)	$w \sim Wishart(\Sigma_{\vartheta}\,/2,2)$

Table 1. Hyperparameters of the infinite Gaussian mixture model and the associated priors used in our analysis. $\mu_{\vartheta}, \Sigma_{\vartheta}$ are obtained in the first step of our algorithm as the mean and covariance matrix of the model parameters values, $(u_{gluc,i}^{(1)}, d_{gluc,i}^{(1)})$, obtained via maximum likelihood estimation.

ACKNOWLEDGMENTS

G.G. was supported by an EPSRC DTP PhD studentship (EP/M506527/1). M.V. and K.T.A. gratefully acknowledge financial support from the EPSRC (EP/N014391/1). U.L. was supported through a BBSRC grant (BB/V008021/1) and an MRC Proximity to Discovery EXCITEME2 grant (MCPC17189). This work was further supported by a Royal Society Research Grant (RG180007) awarded to S.P. and a QUEX Initiator grant awarded to S.P. and K.T.A.. D.S.M., T.A.R. and S.P.'s work in this area is also supported by a Marie Skłodowska-Curie project SINGEK (H2020-MSCA-ITN-2015-675752) and the Gordon and Betty Moore Foundation Marine Microbiology Initiative (GBMF5514). B.M.I. acknowledges support from a Wellcome Trust Institutional Strategic Support Award to the University of Exeter (204909/Z/16/Z). This project utilised equipment funded by the Wellcome Trust Institutional Strategic Support Fund (WT097835MF), Wellcome Trust Multi User Equipment Award (WT101650MA) and BBSRC LOLA award (BB/K003240/1).

AUTHOR CONTRIBUTIONS

S.P. designed the research and developed the project. G.G. and U.L. performed the experiments. M.V. and K.T.A. developed and implemented the mathematical model. B.M.I. performed the clustering and gene ontology analysis. D.S., P.O. and K.M performed the transcriptomics analysis. S.R. and D.S.M. assisted G.G. during protein extraction, flow cytometry and colorimetric assays. K.H. performed the proteomics and phosphoproteomics analysis. G.G., M.V., U.L., B.M.I., D.S., N.N., D.S.M., S.R., K.H., P.G.P. T.A.R. and S.P. analysed the data. G.G. and S.P. wrote the paper. All authors read and approved the final manuscript.

963 **COMPETING INTERESTS**

964 The authors declare that they have no competing interests.

965

966 **REFERENCES**

967 1. Delgado-Baquerizo M, Oliverio AM, Brewer TE, Benavent-González A, Eldridge DJ,
968 Bardgett RD, et al. A global atlas of the dominant bacteria found in soil. Science (80-
969). 2018;359: 320–325. doi:10.1126/science.aap9516

970 2. Morita RY. Starvation survival. Bacteria in oligotrophic environments. New York:
971 Chapman & Hall; 1997.

972 3. Cordero OX, Polz MF. Explaining microbial genomic diversity in light of evolutionary
973 ecology. Nature Reviews Microbiology. Nature Publishing Group; 2014. pp. 263–273.
974 doi:10.1038/nrmicro3218

975 4. Eisenreich W, Dandekar T, Heesemann J, Goebel W. Carbon metabolism of
976 intracellular bacterial pathogens and possible links to virulence. Nat Rev Microbiol.
977 2010;8: 401–412. doi:10.1038/nrmicro2351

978 5. Natarajan A, Srienc F. Dynamics of glucose uptake by single Escherichia coli cells.
979 Metab Eng. 1999;1: 320–33. doi:10.1006/mben.1999.0125

980 6. Schaefer U, Boos W, Takors R, Weuster-Botz D. Automated sampling device for
981 monitoring intracellular metabolite dynamics. Anal Biochem. 1999;270: 88–96.
982 doi:10.1006/abio.1999.4048

983 7. Braissant O, Astasov-Frauenhoffer M, Waltimo T, Bonkat G. A Review of Methods to
984 Determine Viability, Vitality, and Metabolic Rates in Microbiology. Front Microbiol.
985 2020;11: 1–25. doi:10.3389/fmicb.2020.547458

986 8. Jahreis K, Pimentel-Schmitt EF, Brückner R, Titgemeyer F. Ins and outs of glucose
987 transport systems in eubacteria. FEMS Microbiol Rev. 2008;32: 891–907.

988 doi:10.1111/j.1574-6976.2008.00125.x
989 9. Yang J-N, Wang C, Guo C, Peng X-X, Li H. Outer membrane proteome and its
990 regulation networks in response to glucose concentration changes in Escherichia coli.
991 Mol Biosyst. 2011;7: 3087–3093. doi:10.1039/c1mb05193h
992 10. Nikaido H. Molecular basis of bacterial outer membrane permeability revisited.
993 Microbiol Mol Biol Rev. 2003;67: 593–656. doi:10.1128/MMBR.67.4.593
994 11. Pratt LA, Hsing W, Gibson KE, Silhavy TJ. From acids to osmZ: Multiple factors
995 influence synthesis of the OmpF and OmpC porins in Escherichia coli. Molecular
996 Microbiology. John Wiley & Sons, Ltd; 1996. pp. 911–917. doi:10.1111/j.1365-
997 2958.1996.tb02532.x
998 12. Chubiz LM, Rao C V. Role of the mar-sox-rob regulon in regulating outer membrane
999 porin expression. J Bacteriol. 2011;193: 2252–2260. doi:10.1128/JB.01382-10
1000 13. Gutknecht R, Flükiger K, Lanz R, Erni B. Mechanism of phosphoryl transfer in the
1001 dimeric IIAB(Man) subunit of the Escherichia coli mannose transporter. J Biol Chem.
1002 1999;274: 6091–6096. doi:10.1074/jbc.274.10.6091
1003 14. Causey TB, Zhou S, Shanmugam KT, Ingram LO. Engineering the metabolism of
1004 Escherichia coli W3110 for the conversion of sugar to redox-neutral and oxidized
1005 products: Homoacetate production. Proc Natl Acad Sci U S A. 2003;100: 825–832.
1006 doi:10.1073/pnas.0337684100
1007 15. Natarajan A, Srienc F. Glucose uptake rates of single E. coli cells grown in glucose-
1008 limited chemostat cultures. J Methods Microbiol J Microbiol Methods. 2000;42: 87–
1009 96. doi:10.1016/S0167-7012(00)00180-9
1010 16. Lendenmann U, Egli T. Is Escherichia coli growing in glucose-limited chemostat
1011 culture able to utilize other sugars without lag? Microbiology. 1995;141: 71–78.
1012 doi:10.1099/00221287-141-1-71

1013 17. Herbert D, Kornberg HL. Glucose Transport as Rate-Limiting Step in the Growth of
1014 Escherichia coli on Glucose. Biochem J. 1976.
1015 18. Rocca JD, Simonin M, Blaszczak JR, Ernakovich JG, Gibbons SM, Midani FS, et al.
1016 The Microbiome Stress Project: Toward a global meta-analysis of environmental
1017 stressors and their effects on microbial communities. Front Microbiol. 2019;10.
1018 doi:10.3389/fmicb.2018.03272
1019 19. McMahon MAS, Xu J, Moore JE, Blair IS, McDowell DA. Environmental stress and
1020 antibiotic resistance in food-related pathogens. Appl Environ Microbiol. 2007;73:
1021 211–217. doi:10.1128/AEM.00578-06
1022 20. Boor KJ. Bacterial stress responses: What doesn't kill them can make them stronger.
1023 PLoS Biology. Public Library of Science; 2006. pp. 0018–0020.
1024 doi:10.1371/journal.pbio.0040023
1025 21. Guan N, Li J, Shin H-D, Du G, Chen J, Liu L. Microbial response to environmental
1026 stresses: from fundamental mechanisms to practical applications. doi:10.1007/s00253-
1027 017-8264-y
1028 22. Roszak DB&, Colwell RR. Survival strategies of bacteria in the natural environment.
1029 Clin Microbiol Rev. 1987;51: 365–379.
1030 23. Goldman JC, Dennett MR. Growth of marine bacteria in batch and continuous culture
1031 under carbon and nitrogen limitation. Limnol Oceanogr. 2000;45: 789–800.
1032 24. Caglar MU, Houser JR, Barnhart CS, Boutz DR, Carroll SM, Dasgupta A, et al. The E.
1033 coli molecular phenotype under different growth conditions. Sci Rep. 2017;7: 45303.
1034 doi:10.1038/srep45303
1035 25. Canedo-Arguelles M, Hawkins CP, Kefford BJ, Schafer RB, Dyack BJ, Brucet S, et al.
1036 Saving freshwater from salts. Science (80-). 2016;351: 914–916.
1037 doi:10.1126/science.aad3488

1038 26. Millennium Ecosystem Assessment. Ecosystems and Human Well-being: Synthesis.
1039 Isl Press Washington, DC. 2005. Available: http://www.bioquest.org/wp-
1040 content/blogs.dir/files/2009/06/ecosystems-and-health.pdf
1041 27. Prayitno SB, Latchford JW. Experimental infections of crustaceans with luminous
1042 bacteria related to Photobacterium and Vibrio. Effect of salinity and pH on infectiosity.
1043 Aquaculture. 1995;132: 105–112.
1044 28. Singleton FL, Attwell RW, Jangi MS, Colwell RR. Influence of salinity and organic
1045 nutrient concentration on survival and growth of Vibrio cholerae in aquatic
1046 microcosms. Appl Environ Microbiol. 1982;43: 1080–1085.
1047 29. Cañedo-Argüelles M, Kefford BJ, Piscart C, Prat N, Schäfer RB, Schulz CJ.
1048 Salinisation of rivers: An urgent ecological issue. Environ Pollut. 2013;173: 157–167.
1049 doi:10.1016/j.envpol.2012.10.011
1050 30. Holliday NP, Bersch M, Berx B, Chafik L, Cunningham S, Florindo-López C, et al.
1051 Ocean circulation causes the largest freshening event for 120 years in eastern subpolar
1052 North Atlantic. Nat Commun. 2020;11. doi:10.1038/s41467-020-14474-y
1053 31. Müsken A, Bielaszewska M, Greune L, Schweppe CH, Müthing J, Schmidt H, et al.
1054 Anaerobic conditions promote expression of Sfp fimbriae and adherence of sorbitol-
1055 fermenting enterohemorrhagic Escherichia coli O157:NM to human intestinal
1056 epithelial cells. Appl Environ Microbiol. 2008;74: 1087–1093.
1057 doi:10.1128/AEM.02496-07
1058 32. Polzin S, Huber C, Eylert E, Elsenhans I, Eisenreich W, Schmidt H. Growth media
1059 simulating ileal and colonic environments affect the intracellular proteome and carbon
1060 fluxes of enterohemorrhagic escherichia coli O157: H7 strain EDL933. Appl Environ
1061 Microbiol. 2013;79: 3703–3715. doi:10.1128/AEM.00062-13
1062 33. Beumer RR, de Vries J, Rombouts FM. Campylobacter jejuni non-culturable coccoid

1063 cells. Contrib Microbiol. 2001;8: 150–165. doi:10.4324/9780203856871-3
1064 34. Grandjean Lapierre S, Phelippeau M, Hakimi C, Didier Q, Reynaud-Gaubert M,
1065 Dubus JC, et al. Cystic fibrosis respiratory tract salt concentration: An exploratory
1066 cohort study. Med (United States). 2017;96: 1–4. doi:10.1097/MD.0000000000008423
1067 35. Velasco J, Gutiérrez-Cánovas C, Botella-Cruz M, Sánchez-Fernández D, Arribas P,
1068 Carbonell JA, et al. Effects of salinity changes on aquatic organisms in a multiple
1069 stressor context. Philos Trans R Soc B Biol Sci. 2019;374: 20180011.
1070 doi:10.1098/rstb.2018.0011
1071 36. Jang J, Hur HG, Sadowsky MJ, Byappanahalli MN, Yan T, Ishii S. Environmental
1072 Escherichia coli: ecology and public health implications—a review. J Appl Microbiol.
1073 2017;123: 570–581. doi:10.1111/jam.13468
1074 37. Chubukov V, Desmarais JJ, Wang G, Chan LJG, Baidoo EEK, Petzold CJ, et al.
1075 Engineering glucose metabolism of escherichia coli under nitrogen starvation. npj Syst
1076 Biol Appl. 2017;3: 1–7. doi:10.1038/npjsba.2016.35
1077 38. Nestorovich EM, Danelon C, Winterhalter M, Bezrukov SM. Designed to penetrate:
1078 Time-resolved interaction of single antibiotic molecules with bacterial pores. Proc Natl
1079 Acad Sci U S A. 2002;99: 9789–9794. doi:10.1073/pnas.152206799
1080 39. Cama J, Voliotis M, Metz J, Smith A, Iannucci J, Keyser UF, et al. Single-cell
1081 microfluidics facilitates the rapid quantification of antibiotic accumulation in Gram-
1082 negative bacteria. Lab Chip. 2020;20: 2765–2775. doi:10.1039/d0lc00242a
1083 40. Łapińska U, Voliotis M, Lee KK, Campey A, Stone MRL, Phetsang W, et al. Fast
1084 bacterial growth reduces antibiotic accumulation and efficacy. Biorxiv. 2021.
1085 doi:10.1101/2021.10.18.464851v1
1086 41. Wang P, Robert L, Pelletier J, Dang WL, Taddei F, Wright A, et al. Robust growth of
1087 Escherichia coli. Curr Biol. 2010;20: 1099–1103. doi:10.1016/j.cub.2010.04.045

1088 42. Yoshioka K, Saito M, Oh K-B, Nemoto Y, Abe H, Matsuoka H, et al. Intracellular
1089 Fate of 2-NBDG, a Fluorescent Probe for Glucose Uptake Activity, in Escherichia coli
1090 Cells. Biosci Biotechnol Biochem. 2009;60: 1899–1901. doi:10.1271/bbb.60.1899
1091 43. Yoshioka K, Takahashi H, Homma T, Saito M, Oh KB, Nemoto Y, et al. A novel
1092 fluorescent derivative of glucose applicable to the assessment of glucose uptake
1093 activity of Escherichia coli. Biochim Biophys Acta - Gen Subj. 1996;1289: 5–9.
1094 doi:10.1016/0304-4165(95)00153-0
1095 44. Şimşek E, Kim M. The emergence of metabolic heterogeneity and diverse growth
1096 responses in isogenic bacterial cells. ISME J. 2018. doi:10.1038/s41396-017-0036-2
1097 45. Wee S, Wilkinson BJ. Increased outer membrane ornithine-containing lipid and
1098 lysozyme penetrability of Paracoccus denitrificans grown in a complex medium
1099 deficient in divalent cations. J Bacteriol. 1988;170: 3283–3286.
1100 doi:10.1128/jb.170.7.3283-3286.1988
1101 46. Maguire ME, Papp-Wallace KM. Magnesium Transport and Magnesium Homeostasis.
1102 EcoSal Plus. 2008;3. doi:10.1128/ecosalplus.5.4.4.2
1103 47. Battesti A, Majdalani N, Gottesman S. The RpoS-Mediated General Stress Response
1104 in *Escherichia coli*. Annu Rev Microbiol. 2011;65: 189–213. doi:10.1146/annurev-
1105 micro-090110-102946
1106 48. Sugimoto S, Arita-Morioka KI, Mizunoe Y, Yamanaka K, Ogura T. Thioflavin T as a
1107 fluorescence probe for monitoring RNA metabolism at molecular and cellular levels.
1108 Nucleic Acids Res. 2015;43: 1–12. doi:10.1093/nar/gkv338
1109 49. Bieler S, Estrada L, Lagos R, Baeza M, Castilla J, Soto C. Amyloid formation
1110 modulates the biological activity of a bacterial protein. J Biol Chem. 2005;280: 26880–
1111 26885. doi:10.1074/jbc.M502031200
1112 50. Metris A, George SM, Mulholland F, Carter AT, Baranyi J. Metabolic shift of

1113 Escherichia coli under salt stress in the presence of glycine betaine. Appl Environ
1114 Microbiol. 2014;80: 4745–4756. doi:10.1128/AEM.00599-14
1115 51. Nikaido H. The limitations of LB medium. In: Small things considered - American
1116 Society of Microbiology. 2009.
1117 52. Li SHJ, Li Z, Park JO, King CG, Rabinowitz JD, Wingreen NS, et al. Escherichia coli
1118 translation strategies differ across carbon, nitrogen and phosphorus limitation
1119 conditions. Nat Microbiol. 2018;3: 939–947. doi:10.1038/s41564-018-0199-2
1120 53. Taniguchi Y, Choi PJ, Li G-W, Chen H, Babu M, Hearn J, et al. Quantifying E. coli
1121 proteome and transcritpome with single-molecule sensitivity in single cells. Science
1122 (80-). 2010;329: 533–538.
1123 54. Smith A, Kaczmar A, Bamford RA, Smith C, Frustaci S, Kovacs-Simon A, et al. The
1124 culture environment influences both gene regulation and phenotypic heterogeneity in
1125 Escherichia coli. Front Microbiol. 2018;9: 1739. doi:10.3389/fmicb.2018.01739
1126 55. Soares NC, Spät P, Krug K, MacEk B. Global dynamics of the Escherichia coli
1127 proteome and phosphoproteome during growth in minimal medium. J Proteome Res.
1128 2013;12: 2611–2621. doi:10.1021/pr3011843
1129 56. Fu L, Bounelis P, Dey N, Browne BL, Marchase RB, Bedwell DM. The
1130 posttranslational modification of phosphoglucomutase is regulated by galactose
1131 induction and glucose repression in Saccharomyces cerevisiae. J Bacteriol. 1995;177:
1132 3087–3094. doi:10.1128/jb.177.11.3087-3094.1995
1133 57. Lu M, Kleckner N. Molecular cloning and characterization of the pgm gene encoding
1134 phosphoglucomutase of Escherichia coli. J Bacteriol. 1994;176: 5847–5851.
1135 doi:10.1128/jb.176.18.5847-5851.1994
1136 58. Brown CW, Sridhara V, Boutz DR, Person MD, Marcotte EM, Barrick JE, et al.
1137 Large-scale analysis of post-translational modifications in E.coli under glucose-

1138 limiting conditions. BMC Genomics. 2017;18: 1–21. doi:10.1186/s12864-017-3676-8
1139 59. Stiers, K. M.; Muenks, A. G.; Beamer LJ. Biology, mechanism, and structure of
1140 enzymes in the α-D-phosphohexomutase superfamily. Adv Protein Chem Struct Biol.
1141 2017;176: 139–148. doi:10.1016/bs.apcsb.2017.04.005.Biology
1142 60. Hunter IS, Kornberg HL. Glucose transport of Escherichia coli growing in glucose-
1143 limited continuous culture. Biochem J. 1979;178: 97–101. doi:10.1042/bj1780097
1144 61. Macek B, Forchhammer K, Hardouin J, Weber-Ban E, Grangeasse C, Mijakovic I.
1145 Protein post-translational modifications in bacteria. Nat Rev Microbiol. 2019;17: 651–
1146 664. doi:10.1038/s41579-019-0243-0
1147 62. Bren A, Park JO, Towbin BD, Dekel E, Rabinowitz JD, Alon U. Glucose becomes one
1148 of the worst carbon sources for E.coli on poor nitrogen sources due to suboptimal
1149 levels of cAMP. Sci Rep. 2016;6: 1–10. doi:10.1038/srep24834
1150 63. Yannarell AC, Paerl HW. Effects of salinity and light on organic carbon and nitrogen
1151 uptake in a hypersaline microbial mat. FEMS Microbiol Ecol. 2007;62: 345–353.
1152 doi:10.1111/j.1574-6941.2007.00384.x
1153 64. Griffiths RP, Morita RY. Salinity effects on glucose uptake and catabolism in the
1154 obligately psychrophilic marine bacterium Vibrio marinus. Mar Biol. 1973;23: 177–
1155 182. doi:10.1007/BF00389482
1156 65. Weber A, Kögl SA, Jung K. Time-dependent proteome alterations under osmotic stress
1157 during aerobic and anaerobic growth in Escherichia coli. J Bacteriol. 2006;188: 7165–
1158 7175. doi:10.1128/JB.00508-06
1159 66. Abdulkarim SM, Fatimah AB, Anderson JG. Effect of salt concentrations on the
1160 growth of heat-stressed and unstressed Escherichia coli. J Food, Agric Environ.
1161 2009;7: 51–54.
1162 67. Jõers A, Tenson T. Growth resumption from stationary phase reveals memory in

1163 Escherichia coli cultures. Sci Rep. 2016;6: 1–11. doi:10.1038/srep24055
1164 68. Scott M, Gunderson CW, Mateescu EM, Zhang Z, Hwa T. Interdependence of cell
1165 growth and gene expression: Origins and consequences. Science (80-). 2010;330:
1166 1099–1102. doi:10.1126/science.1192588
1167 69. Taheri-Araghi S, Bradde S, Sauls JT, Hill NS, Levin PA, Paulsson J, et al. Cell-size
1168 control and homeostasis in bacteria. Curr Biol. 2015;25: 385–391.
1169 doi:10.1016/j.cub.2014.12.009
1170 70. O'Brien EJ, Lerman JA, Chang RL, Hyduke DR, Palsson BØ. Genome-scale models
1171 of metabolism and gene expression extend and refine growth phenotype prediction.
1172 Mol Syst Biol. 2013;9: 693. doi:10.1038/msb.2013.52
1173 71. Wallden M, Fange D, Lundius EG, Baltekin Ö, Elf J. The Synchronization of
1174 Replication and Division Cycles in Individual E. coli Cells. Cell. 2016;166: 729–739.
1175 doi:10.1016/j.cell.2016.06.052
1176 72. Deforet M, Van Ditmarsch D, Xavier JB. Cell-Size Homeostasis and the Incremental
1177 Rule in a Bacterial Pathogen. Biophys J. 2015;109: 521–528.
1178 doi:10.1016/j.bpj.2015.07.002
1179 73. Bamford RA, Smith A, Metz J, Glover G, Titball RW, Pagliara S. Investigating the
1180 physiology of viable but non-culturable bacteria by microfluidics and time-lapse
1181 microscopy. BMC Biol. 2017;15: 121. doi:10.1186/s12915-017-0465-4
1182 74. Nikolic N, Schreiber F, Dal Co A, Kiviet DJ, Bergmiller T, Littmann S, et al. Cell-to-
1183 cell variation and specialization in sugar metabolism in clonal bacterial populations.
1184 PLoS Genet. 2017;13: 1–24. doi:10.1371/journal.pgen.1007122
1185 75. Nikolic N, Barner T, Ackermann M. Analysis of fluorescent reporters indicates
1186 heterogeneity in glucose uptake and utilization in clonal bacterial populations. BMC
1187 Microbiol. 2013;13: 258. doi:10.1186/1471-2180-13-258

1188 76. Ackermann M. A functional perspective on phenotypic heterogeneity in
1189 microorganisms. Nat Rev Microbiol. 2015;13: 497–508. doi:10.1038/nrmicro3491
1190 77. Richards TA, Massana R, Pagliara S, Hall N. Single cell ecology. Philos Trans R Soc
1191 B Biol Sci. 2019;374: 20190076.
1192 78. Stone MRL, Łapińska U, Pagliara S, Masi M, Blanchfield JT, Cooper MA, et al.
1193 Fluorescent macrolide probes – synthesis and use in evaluation of bacterial resistance.
1194 RSC Chem Biol. 2020;1: 395–404. doi:10.1039/d0cb00118j
1195 79. Takhaveev V, Heinemann M. Metabolic heterogeneity in clonal microbial populations.
1196 Curr Opin Microbiol. 2018;45: 30–38. doi:10.1016/j.mib.2018.02.004
1197 80. Zimmermann M, Escrig S, Hübschmann T, Kirf MK, Brand A, Inglis RF, et al.
1198 Phenotypic heterogeneity in metabolic traits among single cells of a rare bacterial
1199 species in its natural environment quantified with a combination of flow cell sorting
1200 and NanoSIMS. Front Microbiol. 2015;6: 1–11. doi:10.3389/fmicb.2015.00243
1201 81. Nielsen JL, Christensen D, Kloppenborg M, Halkjær Nielsen P. Quantification of cell-
1202 specific substrate uptake by probe-defined bacteria under in situ conditions by
1203 microautoradiography and fluorescence in situ hybridization. Environ Microbiol.
1204 2003;5: 202–211. doi:10.1046/j.1462-2920.2003.00402.x
1205 82. Sintes E, Herndl GJ. Quantifying substrate uptake by individual cells of marine
1206 bacterioplankton by catalyzed reporter deposition fluorescence in situ hybridization
1207 combined with microautoradiography. Appl Environ Microbiol. 2006;72: 7022–7028.
1208 doi:10.1128/AEM.00763-06
1209 83. Lapinska U, Glover G, Capilla-lasheras P, Young AJ, Pagliara S. Bacterial ageing in
1210 the absence of external stressors. Philos Trans R Soc B Biol Sci. 2019;374: 20180442.
1211 84. Kopf SH, McGlynn SE, Green-Saxena A, Guan Y, Newman DK, Orphan VJ. Heavy
1212 water and 15N labelling with NanoSIMS analysis reveals growth rate-dependent

metabolic heterogeneity in chemostats. Environ Microbiol. 2015;17: 2542–2556. doi:10.1111/1462-2920.12752

85. Kepiro IE, Marzuoli I, Hammond K, Ba X, Lewis H, Shaw M, et al. Engineering Chirally Blind Protein Pseudocapsids into Antibacterial Persisters. ACS Nano. 2020;14: 1609. doi:10.1021/acsnano.9b06814

86. Attrill EL, Claydon R, Łapińska U, Recker M, Meaden S, Brown AT, et al. Individual bacteria in structured environments rely on phenotypic resistance to phage. PLOS Biol. 2021;19: e3001406. doi:10.1371/journal.pbio.3001406

87. Yoshioka K, Oh K-B, Saito • M, Nemoto • Y, Matsuoka H. Evaluation of 2-[N-(7-nitrobenz-2-oxa-l,3-diazol-4-yl)amino]-2-deoxy-D. glucose, a new fluorescent derivative of glucose, for viability assessment of yeast Candida albicans. Appl Microbic Biotechnol. 1996.

88. Goode O, Smith A, Łapińska U, Attrill E, Carr A, Metz J, et al. Heterologous Protein Expression Favors the Formation of Protein Aggregates in Persister and Viable but Nonculturable Bacteria ́. ACS Infect Dis. 2021;7: 1848. doi:10.1021/acsinfecdis.1c00154

89. Dettmer SL, Keyser UF, Pagliara S. Local characterization of hindered Brownian motion by using digital video microscopy and 3D particle tracking. Rev Sci Instrum. 2014;85. doi:10.1063/1.4865552

90. Locatelli E, Pierno M, Baldovin F, Orlandini E, Tan Y, Pagliara S. Single-File Escape of Colloidal Particles from Microfluidic Channels. Phys Rev Lett. 2016;117: 038001. doi:10.1103/PhysRevLett.117.038001

91. Smith A, Metz J, Pagliara S. MMHelper : An automated framework for the analysis of microscopy images acquired with the mother machine. Sci Rep. 2019;9: 10123. doi:10.1038/s41598-019-46567-0

1238 92. Goode O, Smith A, Zarkan A, Cama J, Invergo BM, Belgami D, et al. Persister
1239 Escherichia coli Cells Have a Lower Intracellular pH than Susceptible Cells but
1240 Maintain Their pH in Response to. MBio. 2021;12: e00909-21.
1241 93. Love MI, Huber W, Anders S. Moderated estimation of fold change and dispersion for
1242 RNA-seq data with DESeq2. Genome Biol. 2014;15: 550. doi:10.1186/s13059-014-
1243 0550-8
1244 94. Phipson B, Lee S, Majewski IJ, Alexander WS, Smyth G. Robust Hyperparameter
1245 Estimation Protects. Ann Appl Stat. 2016;10: 946–963. doi:10.1214/16-
1246 AOAS920.ROBUST
1247 95. Kammers K, Cole RN, Tiengwe C, Ruczinski I. Detecting significant changes in
1248 protein abundance. EuPA Open Proteomics. 2015;7: 11–19.
1249 doi:10.1016/j.euprot.2015.02.002
1250 96. Benjamini Y, Hochberg Y. Controlling the False Discovery Rate: A Practical and
1251 Powerful Approach to Multiple Testing. J R Stat Soc B. 1995;57: 289–300.
1252 97. Scrucca L, Fop M, Murphy BT, Raftery AE. mclust 5: Clustering, Classification and
1253 Density Estimation Using. R J. 2016;8: 289–317.
1254 98. Yu G, Wang LG, Han Y, He QY. ClusterProfiler: An R package for comparing
1255 biological themes among gene clusters. Omi A J Integr Biol. 2012;16: 284–287.
1256 doi:10.1089/omi.2011.0118
1257 99. Rasmussen CE. The Infinite Gaussian Mixture Model.
1258
1259
1260
1261
1262

1263 **SUPPLEMENTAL INFORMATION**

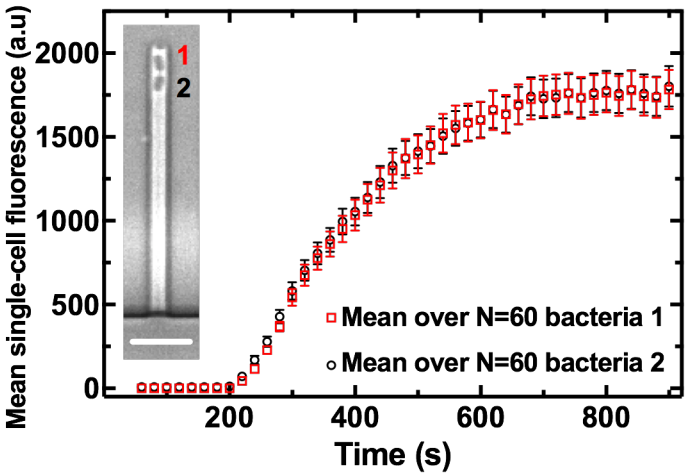

1264
1265 **Figure S1.** Temporal dependence of the mean intracellular fluorescence of the glucose
1266 analogue 2-NBDG averaged over 60 individual *E. coli* at the top of each dead-end bacteria-
1267 hosting channel (red squares, position 1) or below such cells (black circles, position 2). Bacteria
1268 at position 2 are closer to the main microfluidic chamber i.e. the 2-NBDG source, whereas
1269 bacteria at position 1 are screened by one cell. Statistical comparisons are reported in Table S1.
1270 Inset: bright-field microscopy image illustrating bacteria in positions 1 and 2, scale bar: 5 µm.
1271
1272

Time (s)	t ratio	df	*p*- value
0			
100	1,26	58	0,21
200	1,60	58	0,11
300	0,52	58	0,60
400	0,18	58	0,86
500	0,12	58	0,91
600	0,01	58	0,99
700	0,11	58	0,92
800	0,07	58	0,94
900	0,11	58	0,91

1273
1274 **Table S1.** Statistical comparisons of 2-NBDG accumulation in *E. coli* at the top of each dead-
1275 end bacteria-hosting channel or below such cells (positions 1 and 2 in Fig. S1, respectively).
1276

Time (s)	Optimal growth conditions		Nutrient depletion	
	Mean fluorescence (a.u.)	CV fluorescence (%)	Mean fluorescence (a.u.)	CV fluorescence (%)
0	0	0	0	0
100	17	48	22	61
200	37	90	40	49
300	250	46	417	58
400	435	35	546	58
500	533	33	647	55
600	613	32	692	57
700	685	32	762	55
800	699	33	769	58
900	733	32	740	60
1000	730	34	683	54
1100	761	32	663	59
1200	580	46	458	54
1300	350	47	293	61
1400	231	49	208	64
1500	156	52	150	67
1600	112	52	113	69
1700	83	55	91	67
1800	63	55	76	69
1900	53	53	64	64
2000	42	47	51	64
Time (s)	Salt depletion		Nutrient and salt depletion	
	Mean fluorescence (a.u.)	CV fluorescence (%)	Mean fluorescence (a.u.)	CV fluorescence (%)
0	0	0	0	0
100	12	86	12	86
200	13	84	16	90
300	148	70	722	43
400	262	45	1208	42
500	298	43	1507	40
600	332	39	1669	38
700	326	41	1648	39
800	317	43	1676	38
900	373	39	1714	38
1000	393	43	1583	39
1100	429	38	1670	38
1200	328	45	1146	46
1300	155	38	582	55
1400	83	50	341	64
1500	44	98	186	55
1600	34	118	124	60
1700	23	128	82	79
1800	25	143	53	70
1900	29	151	40	62
2000	18	169	27	71

Table S2. Temporal dependence of the mean and coefficient of variation of intracellular fluorescence of the glucose analogue 2-NBDG over at least 30 individual *E. coli* (collated from biological triplicate) per environmental condition as detailed in Figure 2.

Time (s)	Nutrient depletion		
	t ratio	df	*p*-value
0			
100	2,07	112,00	0,04
200	0,45	112,00	0,65
300	4,96	112,00	$<10^{-5}$
400	2,53	112,00	0,01
500	2,27	112,00	0,03
600	1,43	112,00	0,15
700	0,30	112,00	0,20
800	1,11	112,00	0,27
900	0,12	112,00	0,90
Time (s)	**Salt depletion**		
	t ratio	**df**	***p*-value**
0			
100	3,46	166,00	$<10^{-3}$
200	6,43	166,00	$<10^{-6}$
300	5,89	166,00	$<10^{-6}$
400	7,94	166,00	$<10^{-6}$
500	9,47	166,00	$<10^{-6}$
600	10,74	166,00	$<10^{-6}$
700	12,05	146,00	$<10^{-6}$
800	12,35	146,00	$<10^{-6}$
900	11,11	146,00	$<10^{-6}$
Time (s)	**Nutrient and salt depletion**		
	t ratio	**df**	***p*-value**
0			
100	3,39	120,00	$<10^{-3}$
200	3,99	120,00	$<10^{-4}$
300	11,91	120,00	$<10^{-6}$
400	12,33	120,00	$<10^{-6}$
500	13,14	120,00	$<10^{-6}$
600	13,55	120,00	$<10^{-6}$
700	11,89	110,00	$<10^{-6}$
800	11,96	110,00	$<10^{-6}$
900	11,60	110,00	$<10^{-6}$

Table S3. Statistical comparisons of 2-NBDG accumulation in *E. coli* under nutrient, salt or combined nutrient and salt depletion compared to optimal growth conditions.

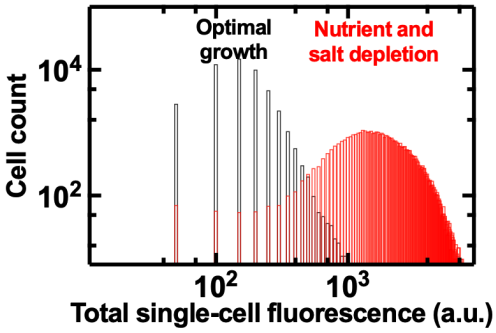

Figure S2. Total intracellular fluorescence of the glucose analogue 2-NBDG in individual *E. coli* under optimal growth conditions and combined nutrient and salt depletion (black and red bars, respectively) measured by flow cytometry after 900s bulk incubation in 2-NBDG. Noteworthy, these measurements were not normalized by cell size.

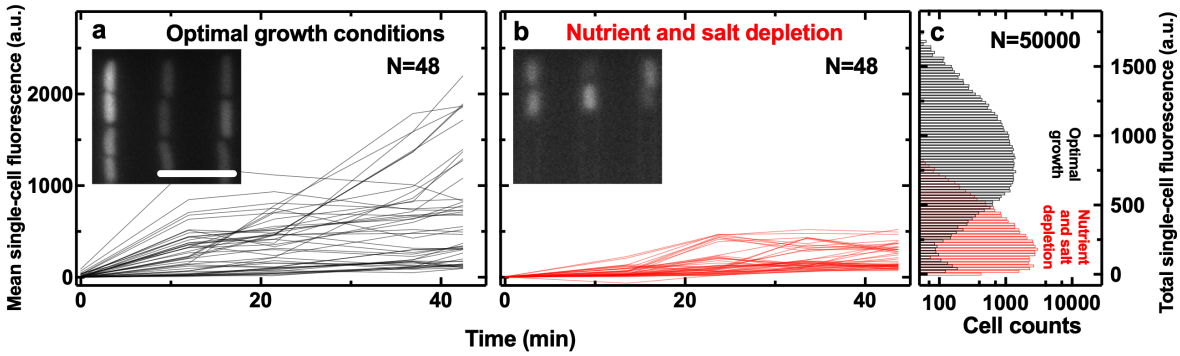

Figure S3. Temporal dependence of the mean intracellular fluorescence of thioflavin T in individual *E. coli* in **a)** optimal growth conditions and **b)** under combined nutrient and salt depletion. Lines are temporal dependences of the intracellular fluorescence of individual bacteria collated from biological triplicate. Noteworthy, we measured thioflavin T fluorescence as the mean fluorescent values of each pixel constituting each bacterium, thus normalizing by cell size. Insets: corresponding fluorescence images at t=45min when the intracellular ThT accumulation has reached saturation levels in individual bacteria. **c)** Corresponding total intracellular fluorescence of thioflavin T under optimal growth conditions or combined nutrient and salt depletion (black and red bars, respectively) measured by flow cytometry after 45min bulk incubation in thioflavin T. Noteworthy, these measurements were not normalized by cell size. Statistical comparisons are reported in Table S4.

Time (min)	Microfluidics-microscopy assay			Flow cytometry assay		
	t ratio	df	*p*-value	t ratio	df	*p*-value
0	3,78	94	$<10^{-6}$			
12	7,98	94	$<10^{-6}$			
22	5,56	94	$<10^{-6}$			
37	6,01	94	$<10^{-6}$			
42	6,23	94	$<10^{-6}$	257,9	99578	$<10^{-6}$

Table S4. Statistical comparisons of thioflavin T accumulation in *E. coli* in optimal growth conditions and under combined nutrient and salt depletion as measured via single-cell microfluidics-microscopy and flow cytometry.

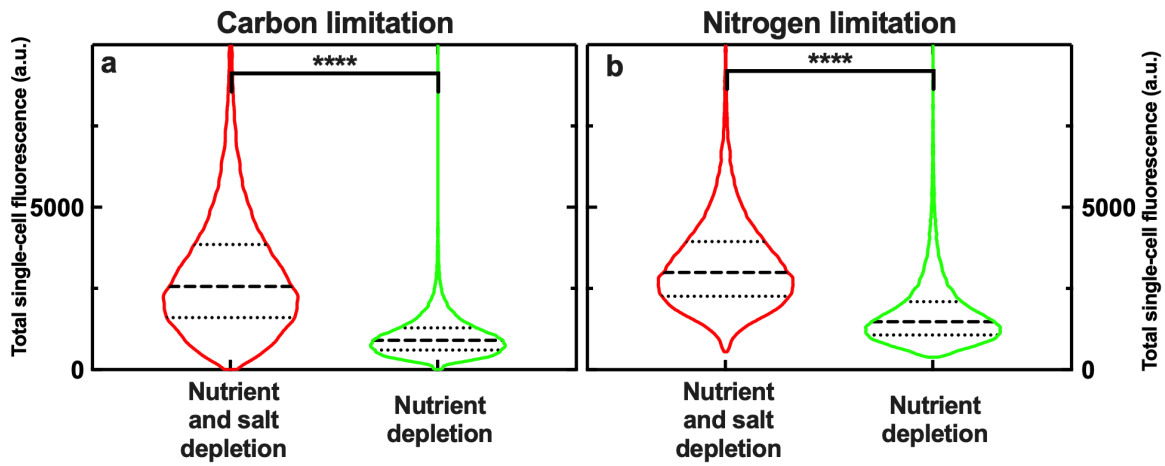

Figure S4. Distribution of total intracellular fluorescence of 2-NBDG under nutrient depletion alone or combined nutrient and salt depletion (green and red violins, respectively) using M9 minimal medium with limited (i.e. 0.1 g/L) **a)** glucose or **b)** ammonia. Measurements were performed on 50,000 bacteria for each environmental condition using flow cytometry after 900s bulk incubation in 2-NBDG. These measurements were not normalized by cell size. ****: p-value <0.0001.

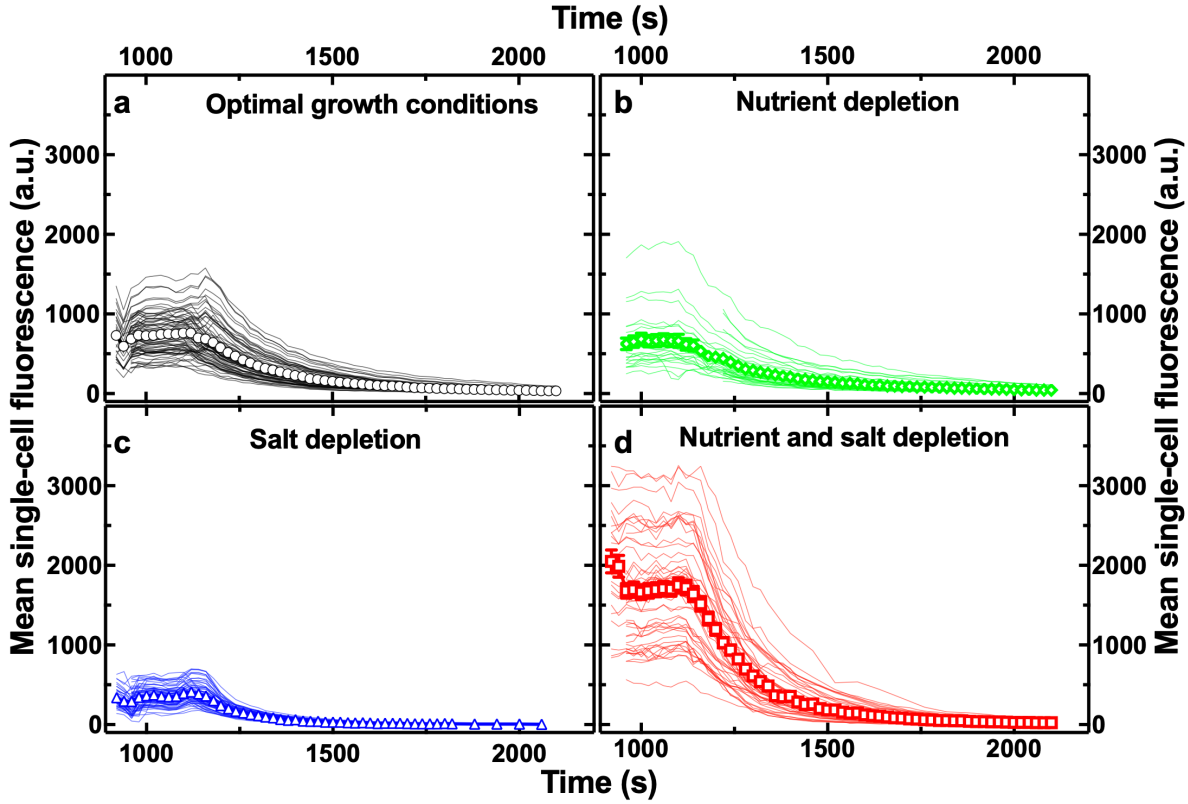

Figure S5. Temporal dependence of the mean intracellular fluorescence of the glucose analogue 2-NBDG in individual *E. coli* under **a)** optimal growth conditions, **b)** nutrient depletion, **c)** salt depletion or **d)** combined nutrient and salt depletion during removal of 2-NBDG from the extracellular environment. Lines are temporal dependences of the intracellular fluorescence of individual bacteria from biological triplicate. Symbols and error bars are the corresponding means and standard error of the means of such single-cell measurements. Means and coefficient of variations of these single-cell values are reported in Table S2. These measurements were normalized by cell size. Measurements were carried out on N=76, 38, 90 and 46 individual bacteria, in a)-d), respectively.

Comparisons with optimal growth	Uptake rate			Degradation rate		
	t ratio	df	*p*-value	t ratio	df	*p*-value
Nutrient depletion	3.88	62,0	0.0003	3.41	42	0.0015
Salt depletion	7.46	116,0	<0.0001	10.97	83	<0.0001
Nutrient and salt depletion	2.59	86,0	0.01	9.30	80	<0.0001

Table S5. Statistical comparisons of the predicted 2-NBDG uptake and degradation values under nutritional, salinity or combined nutritional and salinity depletion compared to optimal growth conditions.

Environment	Uptake rate		Degradation rate	
	Median	CV (%)	Median	CV (%)
Optimal growth conditions	-1,73	13	-2,35	3
Nutrient depletion	-1,94	15	-2,31	9
Salt depletion	-2,05	15	-2,12	9
Nutrient and salt depletion	-1,52	19	-2,18	5

Table S6. Median and coefficient of variation (CV) of the predicted uptake and degradation rate values in optimal growth conditions, under nutritional, salinity or combined nutritional and salinity depletion.

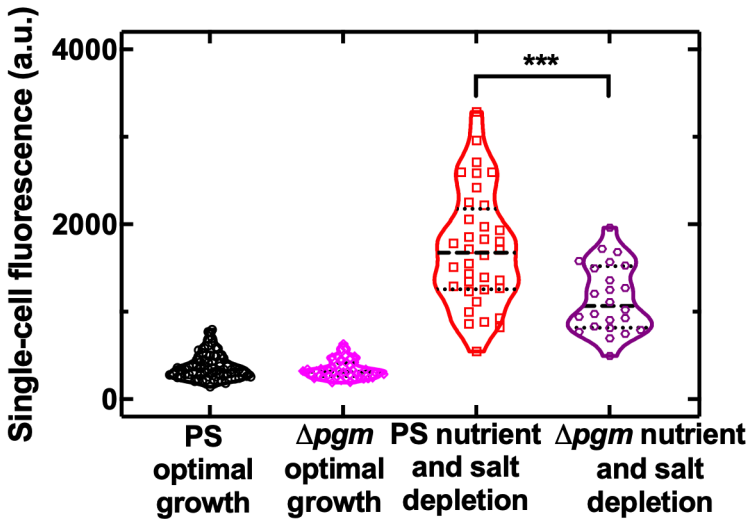

Figure S6. Distribution of single-cell fluorescence after 900 s incubation in 2-NBDG for the parental strain (PS) and Δ*pgm* deletion mutant under salt depletion or simultaneous nutrient and salt depletion. Dashed and dotted lines indicate the median and quartiles of each distribution, respectively. Under nutrient and salt depletion the Δ*pgm* deletion mutant displayed significantly lower 2-NBDG accumulation compared to the parental strain (***). In contrast, under optimal growth conditions the Δ*pgm* deletion mutant displayed 2-NBDG accumulation comparable to the parental strain.

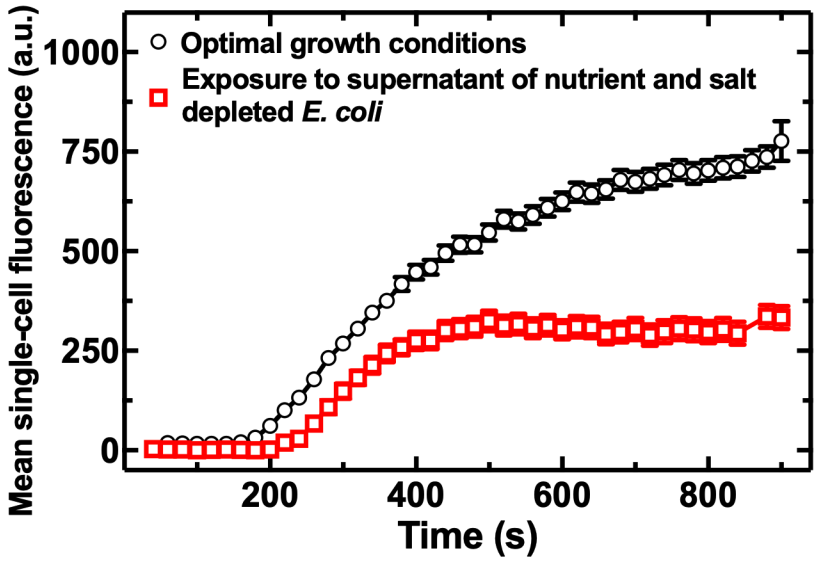

Figure S7. Temporal dependence of the mean intracellular fluorescence of the glucose analogue 2-NBDG in *E. coli* cultured in optimal growth conditions without (circles) or with an additional 1h exposure to the supernatant collected from *E. coli* cultures under combined nutritional and salinity depletion (squares) before 2-NBDG accumulation measurements. Symbols and error bars are the means and standard error of the means over at least 20 single-cell measurements.